The Astrophysical Journal, 903:78 (19pp), 2020 November 10 https://doi.org/10.3847/1538-4357/abba3c

The Evolution of Disk Winds from a Combined Study of Optical and Infrared Forbidden Lines

Ilaria Pascucci[1,2], Andrea Banzatti[3], Uma Gorti[4], Min Fang[5], Klaus Pontoppidan[6], Richard Alexander[7], Giulia Ballabio[7], Suzan Edwards[8], Colette Salyk[9], Germano Sacco[10], Ettore Flaccomio[11], Geoffrey A. Blake[12], Andres Carmona[13], Cassandra Hall[7,14,15], Inga Kamp[16], Hans Ulrich Käufl[17], Gwendolyn Meeus[18,19], Michael Meyer[20], Tyler Pauly[6], Simon Steendam[16], and Michael Sterzik[17]

[1] Lunar and Planetary Laboratory, The University of Arizona, Tucson, AZ 85721, USA; pascucci@lpl.arizona.edu
[2] Earths in Other Solar Systems Team, NASA Nexus for Exoplanet System Science, USA
[3] Department of Physics, Texas State University, 749 N. Comanche Street, San Marcos, TX 78666, USA
[4] SETI Institute/NASA Ames Research Center, Mail Stop 245-3, Moffett Field, CA 94035-1000, USA
[5] California Institute of Technology, Cahill Center for Astronomy and Astrophysics, MC 249-17, Pasadena, CA 91125, USA
[6] Space Telescope Science Institute, 3700 San Martin Drive, Baltimore, MD 21218, USA
[7] School of Physics and Astronomy, University of Leicester, Leicester, LE1 7RH, UK
[8] Five College Astronomy Department, Smith College, Northampton, MA 01063, USA
[9] Department of Physics and Astronomy, Vassar College, 124 Raymond Avenue, Poughkeepsie, NY 12604, USA
[10] INAF—Osservatorio Astrofisico di Arcetri, Largo E. Fermi, 5, I-50125 Firenze, Italy
[11] INAF—Osservatorio Astronomico di Palermo, Piazza del Parlamento 1, I-90134 Palermo, Italy
[12] Division of Geological and Planetary Sciences, California Institute of Technology, Pasadena, CA 91125, USA
[13] Astrophysics & Planetology Research Institute, 9, avenue du Colonel Roche BP 44346 31028 Toulouse Cedex, France 4
[14] Department of Physics and Astronomy, The University of Georgia, Athens, GA 30602, USA
[15] Center for Simulational Physics, The University of Georgia, Athens, GA 30602, USA
[16] Kapteyn Astronomical Institute, University of Groningen, Groningen, The Netherlands
[17] European Southern Observatory, Karl-Schwarzschild-Str. 2, D-85748 Garching, Germany
[18] Department of Theoretical Physics, Autonomous of Madrid, Cantoblanco, E-28049 Madrid, Spain
[19] Centro de Investigación Avanzada en Física Fundamental (CIAFF), Facultad de Ciencias, UAM, E-28049 Madrid, Spain
[20] Department of Astronomy, University of Michigan, 311 West Hall, 1085 S. University Ave., Ann Arbor, MI 48109, USA
Received 2020 June 9; revised 2020 August 26; accepted 2020 September 16; published 2020 November 4

Abstract

We analyze high-resolution ($\Delta v \leqslant 10\,\mathrm{km\,s^{-1}}$) optical and infrared spectra covering the [O I] λ6300 and [Ne II] 12.81 μm lines from a sample of 31 disks in different evolutionary stages. Following work at optical wavelengths, we use Gaussian profiles to fit the [Ne II] lines and classify them into high-velocity component (HVC) or low-velocity component (LVC) if the line centroid is more or less blueshifted than $30\,\mathrm{km\,s^{-1}}$ with respect to the stellar radial velocity, respectively. Unlike for the [O I], where an HVC is often accompanied by an LVC, all 17 sources with an [Ne II] detection have either an HVC or an LVC. [Ne II] HVCs are preferentially detected toward high accretors ($\dot{M}_{\rm acc} > 10^{-8}\,M_{\odot}\,\mathrm{yr^{-1}}$), while LVCs are found in sources with low $\dot{M}_{\rm acc}$, low [O I] luminosity, and large infrared spectral index (n_{13-31}). Interestingly, the [Ne II] and [O I] LVC luminosities display an opposite behavior with n_{13-31}: as the inner dust disk depletes (higher n_{13-31}), the [Ne II] luminosity increases while the [O I] weakens. The [Ne II] and [O I] HVC profiles are generally similar, with centroids and FWHMs showing the expected behavior from shocked gas in microjets. In contrast, the [Ne II] LVC profiles are typically more blueshifted and narrower than the [O I] profiles. The FWHM and centroid versus disk inclination suggest that the [Ne II] LVC predominantly traces unbound gas from a slow, wide-angle wind that has not lost completely the Keplerian signature from its launching region. We sketch an evolutionary scenario that could explain the combined [O I] and [Ne II] results and includes screening of hard (~1 keV) X-rays in inner, mostly molecular, MHD winds.

Unified Astronomy Thesaurus concepts: Protoplanetary disks (1300); Stellar accretion disks (1579); Stellar jets (1607)

1. Introduction

Young (~1–10 Myr) stars are often surrounded by disks of gas and dust within which planets form, hence the term protoplanetary disks. While planet formation contributes to reduce the primordial disk mass, significant mass is removed via accretion of gas through the disk. The final disk clearing is attributed to high-energy stellar photons driving a thermal (also called photoevaporative) wind beyond a few au (e.g., Alexander et al. 2014, for a review), but how disk gas sheds angular momentum to accrete onto the central star remains a crucial, yet unanswered, question.

While MHD disk winds were considered early on (e.g., Pelletier & Pudritz 1992), the prevailing view has been that turbulence driven by magnetorotational instability (MRI; Balbus & Hawley 1991) transports angular momentum outward, enabling disk material to flow radially inward (e.g., Armitage 2011, for a review). However, more recent disk simulations, which include nonideal MHD effects, find that MRI is suppressed in most of the planet-forming region (~1–20 au); hence, accretion is shut off (e.g., Turner et al. 2014, for a review). Corroborating the theoretical results, recent ALMA observations suggest that the majority of the observed disks are weakly turbulent at tens of au (e.g., Teague et al. 2016; Flaherty et al. 2017, 2020). Interestingly, these nonideal MHD simulations persistently predict the presence of disk winds, defined as outflowing gas from a few scale heights above the disk midplane. The simulated winds extract enough

angular momentum to drive accretion at the observed rates (e.g., Gressel et al. 2015, 2020; Bai 2016). These outer winds (beyond a few au out to tens of au in some models), combined with the closer-in winds likely responsible for outflowing gas at hundreds of kilometers per second (hereafter jets; e.g., Frank et al. 2014), could drive disk evolution, with important implications for planet formation and migration (e.g., Ogihara et al. 2018; Kimmig et al. 2020).

Identifying disk winds requires finding gas lines that trace the unbound disk surface at a spectral resolution sufficient enough to detect velocity shifts with respect to Keplerian motion around the star (e.g., Ercolano & Pascucci 2017, for a recent review on disk winds). The first evidence for slow, likely thermal, winds came from high signal-to-noise ratio (S/N), high-resolution ($\Delta v \sim 10\,\mathrm{km\,s^{-1}}$) spectra of [Ne II] at 12.81 μm in three disks with inner dust cavities (Pascucci & Sterzik 2009; Pascucci et al. 2011). The emission lines have modest widths (FWHM $\sim$ 15–40 $\mathrm{km\,s^{-1}}$) and small blueshifts ($\sim$3–6 $\mathrm{km\,s^{-1}}$) in the centroid velocity, compatible with earlier predictions from thermally driven photoevaporative flows (Alexander 2008). Another 10 sources show similar profiles (Baldovin-Saavedra et al. 2012; Sacco et al. 2012), but the lack of sensitive high-resolution mid-infrared spectrographs has so far precluded gathering a diverse and large sample of disks to identify evolutionary trends.

More progress could be made at optical wavelengths. Optical forbidden lines, such as the [O I] at 6300 Å, have long been known to possess a so-called low-velocity component (LVC), emission blueshifted by less than $\sim$30 $\mathrm{km\,s^{-1}}$, in addition to a high-velocity component (HVC) tracing fast ($\sim$100 $\mathrm{km\,s^{-1}}$) collimated microjets (e.g., Hartigan et al. 1995). Early on, Kwan & Tademaru (1995) investigated the possibility that the LVC might trace a slow disk wind. More recently, high-resolution ($\Delta v < 10\,\mathrm{km\,s^{-1}}$) spectroscopy enabled identifying broad wings plus a narrow peak in about half of the LVCs, a profile that has been described as the combination of two Gaussian profiles (a "broad component," BC, and a "narrow component," NC; Rigliaco et al. 2013; Simon et al. 2016; McGinnis et al. 2018). Simon et al. (2016) pointed out that the BC, with its large FWHM, cannot trace a thermal wind beyond a few au but, most likely, probes a closer-in MHD wind. Banzatti et al. (2019) further argued that the entire LVC traces a radially extended MHD wind that feeds a jet based on the finding that the kinematic properties of the BC, peak centroid and FWHM, correlate with those of the NC, and the BC and NC kinematics correlate with the equivalent widths (EWs) of the HVC. However, Weber et al. (2020) recently suggested that these correlations can be explained by a single common correlation between line luminosity and accretion luminosity, with accretion introduced as an EUV component heating the line-emitting region in both their analytic MHD and their X-ray photoevaporative models. They conclude that optical forbidden line profiles are best reproduced by the combination of an inner MHD wind (producing the HVC and BC) and a photoevaporative wind (producing the NC).

Taking advantage of the recent upgrade of VISIR on the VLT (hereafter VISIR 2), our group carried out a large high-resolution spectroscopic survey of protoplanetary disks (PID: 198.C-0104; PI. K. Pontoppidan) focusing on strong rotational lines of water, H_2, and rovibrational lines of OH to investigate disk chemistry, and on the [Ne II] line at 12.81 μm to expand the sample of disk wind sources. Here we focus on the [Ne II] observations and connect the outer winds probed by this infrared forbidden line with the winds traced by the [O I] λ6300 transition, the strongest of the optical forbidden lines (e.g., Hartigan et al. 1995). First, we describe our combined [O I] and [Ne II] disk sample (Section 2) and the detections or upper limits from our VISIR 2 survey (Section 3). Next, we explore whether the known correlations between [O I] luminosities and stellar/disk properties apply to the [Ne II] line luminosities, as well as compare line profiles when both transitions are detected (Section 4). Finally, we discuss our main results, which include evidence for evolution in disk winds (Section 5).

2. Sample and Main Properties

We start from the sample of disks observed with VISIR 2 as part of the Large Program "Protoplanetary disks as chemical factories" (PID: 198.C-0104), which includes 40 sources observed in the [Ne II] 12.81 μm setting.[21] Observations were taken with a slit width of 0.″75, delivering a spectral resolution of $R \sim 30{,}000$ ($\sim$10 $\mathrm{km\,s^{-1}}$), and data were reduced following Banzatti et al. (2014). This large program and the data reduction adapted to the new VISIR detector are described in detail in a forthcoming paper (A. Banzatti et al. 2020, in preparation).

To the VISIR 2 sample we add all other published VISIR 1 spectra of disks covering the [Ne II] line at 12.81 μm, observed at a similar spectral resolution of 10 $\mathrm{km\,s^{-1}}$ (Pascucci & Sterzik 2009; Pascucci et al. 2011; Baldovin-Saavedra et al. 2012; Sacco et al. 2012). Next, we cross-match this list with published [O I] λ6300 detections attained at slightly higher spectral resolution ($R \sim 45{,}000$ or $\sim$7 $\mathrm{km\,s^{-1}}$; Simon et al. 2016; Fang et al. 2018; Banzatti et al. 2019) and found 24 common sources. Similar high-resolution optical spectra for an additional seven disks are retrieved from the archive; their reduction and analysis are described in Appendix A. The resulting sample of 31 disks with [O I] λ6300 detections and VISIR spectra covering the [Ne II] 12.81 μm line is summarized in Table 1. Most of the disks belong to the nearby star-forming regions of Taurus, Lupus, Ophiuchus, Chamaeleon, and Corona Australis.

For each source we collect its Two Micron All Sky Survey (2MASS) equatorial-position-based name and use it to retrieve the Gaia Data Release 2 (hereafter GDR2) parallactic distance from the geometric-distance table generated by Bailer-Jones et al. (2018). No parallax is reported for VW Cha and T CrA; hence, we take as distance that of the star-forming regions the sources belong to: Chamaeleon I (190 pc; Roccatagliata et al. 2018) and Corona Australis (154 pc; Dzib et al. 2018), respectively. Sz 102 and V853 Oph have GDR2 distances that differ significantly from the mean distance of their respective star-forming regions, Lupus and Ophiuchus, but also a high astrometric excess noise. We follow Fang et al. (2018) in using the mean distance to Lupus III and ρ Oph for these two sources, 160 and 138 pc, respectively.

We also collect literature spectral types (SpT), heliocentric radial velocities ($v_{\rm rad}$), stellar luminosities (L_*), mass accretion rates ($\dot{M}_{\rm acc}$), intrinsic X-ray luminosities (L_X), the total luminosity in the [O I] λ6300 line ($L_{[\mathrm{O\,I}]_{\rm tot}}$), and its LVC contribution ($L_{[\mathrm{O\,I}]_{\rm LVC}}$). We scale luminosities and accretion rates to the distances reported in Table 1. Radial velocities are mostly taken from our high-resolution optical surveys (Fang et al. 2018;

[21] This number includes wide binaries extracted separately.

Table 1
VISIR 2 and VISIR 1 Sources with [O I] λ6300 Detections

ID	Target	2MASS	Dist (pc)	SpT	v_{rad} (km s^{-1})	Log L_* ($L_\odot$)	Log $\dot{M}_{acc}$ ($M_\odot$ yr^{-1})	Log L_X ($L_\odot$)	n_{13-31}	Log $L_{[O\ I]tot}$ ($L_\odot$)	Log $L_{[O\ I]LVC}$ ($L_\odot$)	References
VISIR 2												
1	GI Tau	J04333405+2421170	130.0	M0.4	17.1	−0.31	−8.68	−3.82	−0.74	−4.25	−4.44	1,2,3,4
2	HN Tau	J04333935+1751523	136.1	K3	20.8	−0.79	−8.37	−4.10	−0.6	−3.69	⋯	1,2,3,4,5
3	AA Tau	J04345542+2428531	136.7	M0.6	15.4	−0.37	−9.36	−3.60	−0.31	−4.76	−4.84	1,2,3,4
4	DO Tau	J04382858+2610494	138.8	M0.3	17.1	−0.65	−8.22	−4.21	−0.12	−3.76	−4.38	1,2,3,4
5	DR Tau	J04470620+1658428	194.6	K6	23.0	−0.20	−7.81	⋯	−0.33	−4.16	−4.27	1,2,3
6	V836 Tau	J05030659+2523197	168.8	M0.8	20.6	−0.36	−9.4	−3.19	−0.39	−4.78	−4.78	1,2,3,4
7	VW Cha[a]	J11080148–7742288	190.0	K7	14.4	0.36	−7.45	−3.15	−0.17	−3.69	−3.84	6,7,4
8	TWA 3A	J11102788–3731520	36.6	M4.1	12.3	−1.19	−10.15	−4.44	−0.02	−6.09	−6.09	5,2,8
9	GQ Lup	J15491210–3539051	151.2	K6	−2.9	0.17	−7.38	−3.35	−0.22	−4.04	−4.04	9,2,5,4
10	IM Lup	J15560921–3756057	157.7	K5	−0.6	0.41	−8.67	−2.97	−0.3	−4.78	−4.78	9,5,4
11	RU Lup	J15564230–3749154	158.9	K7	0.0	0.17	−6.75	−3.47	−0.58	−3.72	−4.11	9,2,5,4
12	RY Lup	J15592838–4021513	158.4	K2	0.8	0.27	−8.58	−2.62	0.68	−4.63	−4.63	9,2,5,10
13	SR 21	J16271027–2419127	137.9	F7	−5.7	0.99	<−8.39	−3.50	1.82	−4.8	−4.8	5,4
14	RNO 90	J16340916–1548168	116.6	G8	−10.1	0.43	−7.25	⋯	−0.5	−4.16	−4.16	2,5
15	Wa Oph6	J16484562–1416359	123.4	K7	−7.6	−0.12	−7.34	⋯	−0.46	−4.84	⋯	2,5
16	V4046 Sgr[a]	J18141047–3247344	72.3	K5+K7	−6.2	−0.23	−9.22	−3.51	0.87	−5.45	−5.45	11,12,13,14,7
17	S CrA A+B[a]	J19010860–3657200	152.3	K6	2.5	0.25	−7.42	−3.36	0.19	−3.51	⋯	2,5,15
18	TY CrA[a]	J19014081–3652337	136.5	B9	−4.6	1.41	−8.04	−2.84[b]	…[b]	−4.02	⋯	16,17,18,15,7
19	T CrA[a]	J19015878–3657498	154.0	F0	1.1	1.46	−7.94	−5.44	0.91	−3.72	⋯	7,19,18,14
20	VV CrA S[a]	J19030674–3712494	148.8	K7	−5.7	0.33	−6.42	⋯	0.0	−3.05	−3.77	2,5
VISIR 1												
21	LkCa 15	J04391779+2221034	158.2	K5.5	18.7	−0.11	−8.74	−3.00	0.64	−5.05	−5.05	5,1,20
22	TW Hya	J11015191–3442170	60.0	M0.5	13.6	−0.63	−8.67	−3.26	0.68	−4.95	−4.95	5,4,3
23	CS Cha[a]	J11022491–7733357	175.4	K2	15.5	0.24	−8.21	−3.02	2.84	−4.9	−4.9	6,7,4
24	VZ Cha	J11092379–7623207	191.2	M0.5	19.0	−0.1	−7.18	−3.80	−1.07	−4.69	−4.69	6,21,4,22
25	T Cha	J11571348–7921313	109.3	G8	15.8	0.48	−8.11	−3.10	1.33	−4.64	−4.64	23,7,24,4
26	MP Mus	J13220753–6938121	98.6	K1	10.7	−1.13	−8.56	−3.46	0.05	−4.82	−4.82	22,7,14
27	Sz 73	J15475693–3514346	156.1	K7	−3.6	−0.34	−8.53	⋯	−0.1	−4.23	−4.81	9,5
28	Sz 102	J16082972–3903110	160.0	K2	12.0	−0.5	−9.15	−4.52	0.57	−3.75	⋯	5,7,4
29	V853 Oph	J16284527–2428190	138.0	M2.5	−5.8	−0.3	−8.08	−3.01	−0.45	−4.56	−4.76	5,4
30	DoAr 44	J16313346–2427372	145.3	K2	−4.5	−0.02	−8.04	−3.34	−0.45	−4.81	−4.81	5,4
31	RX J1842.9–35	J18425797–3532427	153.2	K3	−0.9	−0.22	−8.51	−3.14	0.64	−4.34	−4.41	5,25

Notes. Stellar luminosities, mass accretion rates, X-ray luminosities, and [O I] λ6300 luminosities are scaled to the distances given in this table. Except for RX J1842.9–35, all L_X are intrinsic, i.e., corrected for absorption, and representative for the energy band 0.3–10 keV. For RX J1842.9–35 the only L_X available is from ROSAT PSPC (0.1–2.4 keV). The spectral index for TWA 3A is actually that for the A+B system, and it is derived from the Spitzer IRAC 8 μm and MIPS 24 μm photometry. Uncertainties in v_{rad} are discussed in Section 2.

[a] Additional notes on complex systems are provided in Appendix B.

[b] The X-ray luminosity of TY CrA is likely dominated by the three later-type companions; no infrared index can be computed owing to uneven nebular background emission (see additional info in Appendix B).

References. (1) Herczeg & Hillenbrand 2014; (2) Banzatti et al. 2019; (3) Simon et al. 2016; (4) Güdel et al. 2010; (5) Fang et al. 2018; (6) Manara et al. 2017; (7) this work; (8) Kastner et al. 2016; (9) Alcalá et al. 2017; (10) Dionatos et al. 2019; (11) Rodriguez et al. 2010; (12) Rosenfeld et al. 2013; (13) Curran et al. 2011; (14) Sacco et al. 2012; (15) Forbrich & Preibisch 2007; (16) Casey et al. 1993; (17) Vioque et al. 2018; (18) Dong et al. 2018; (19) Cazzoletti et al. 2019; (20) Skinner & Güdel 2017; (21) Torres et al. 2006; (22) Rigliaco et al. 2013; (23) Schisano et al. 2009; (24) Cahill et al. 2019; (25) Pascucci et al. 2007.

Banzatti et al. 2019; Appendix A) and have a typical 1σ uncertainty of 1 km s^{-1} (Pascucci et al. 2015). The seven sources with an uncertainty greater than 3 km s^{-1} can be divided into two groups:[22] high accretors like DR Tau with large veiling that reduces the depth of photospheric lines, and extincted/optically faint sources like SR 21 with low-S/N spectra. SR 21 is also the only source in our sample with no detection of accretion-related optical emission lines (Fang et al. 2018); hence, the mass accretion rate in Table 1 is an upper limit. Sz 102 has a nearly edge-on disk; therefore, optical/infrared data largely underestimate its stellar luminosity (Alcalá et al. 2017). However, its stellar mass is known to be $\sim$1.6 $M_{\odot}$ by modeling the ^{12}CO (3–2) Keplerian profile (Louvet et al. 2016). As the source belongs to the Lupus III star-forming region, which is $\sim$2 Myr old (Alcalá et al. 2017), we report in Table 1 the stellar luminosity appropriate for such a star based on the evolutionary models of Baraffe et al. (2015). We use the stellar radius predicted from these models to calculate its mass accretion rate starting from the accretion luminosity reported in Fang et al. (2018). Additional notes on complex systems are provided in Appendix B.

The majority of our sources have [O I] λ6300 LVC emission; only for six disks can the entire emission be attributed to jets (HN Tau, Wa Oph6, S CrA A+B, TY CrA, T CrA, and Sz 102; see Table 1). Note that in several of these cases it is the close-to-edge-on view that precludes us from kinematically separating the LVC from the HVC; see also Appendix A. Among the LVCs, nine have a BC *and* an NC, while the remaining 16 have either a BC *or* an NC. Because of the lower spectral resolution and typically lower S/N of the VISIR spectra, we cannot distinguish additional components within the [Ne II] LVC. Hence, moving forward, we will not discuss the [O I] NC and BC separately but rather combine their luminosities as in Table 1 and only separate the [O I] LVC from the HVC.

To characterize the level of dust depletion in the inner disk, we also calculate the infrared spectral index n_{13-31} defined as in Furlan et al. (2009) and provide it in Table 1. To this end we retrieved fully reduced medium-resolution ($R \sim 700$) Spitzer archival spectra from Pontoppidan et al. (2010) or from the online CASSIS database (Lebouteiller et al. 2015) and used the same wavelength ranges as in Banzatti et al. (2019) to compute the mean flux densities at the relevant wavelengths. The CASSIS database only offers low-resolution Spitzer spectra of MP Mus and V836 Tau, so we use the wavelength ranges adopted in Furlan et al. (2009), appropriate for the lower spectral resolution. Finally, the high-resolution Spitzer spectrum from TWA 3A is of poor quality, with a large discontinuity between the short- and long-wavelength modules. Hence, for this source we use the Spitzer IRAC and MIPS photometry closest to the 13 and 31 μm wavelengths to calculate the spectral index in Table 1. Spectral indices greater than $\sim$0 point to dust depletion and the presence of inner cavities (Furlan et al. 2009). Indeed, the well-known disks with dust cavities around SR 21, LkCa 15, TW Hya, CS Cha, and T Cha (e.g., van der Marel et al. 2016) have relatively large and positive spectral indices.

In addition to this sample of 31 disks observed at high spectral resolution at optical *and* infrared wavelengths, we will include in Section 4.1 five more disks with $n_{13-31} \gtrsim 1$, [O I] detections but no HVC, and medium-resolution ($R \sim 700$) infrared spectra from Spitzer/IRS; see Table 6. As demonstrated in Appendix C using our Table 1 sources, disks with $n_{13-31} \gtrsim 1$ and no [O I] HVC have Spitzer [Ne II] fluxes well within a factor of two of the VISIR ones. Hence, such disks can be used to expand the high-resolution mid-infrared sample.

[22] These sources are DO Tau, DR Tau, HN Tau, RU Lup, VV CrA, SR 21, and Wa Oph6, with a mean uncertainty in $v_{\rm rad}$ of 5 km s^{-1}.

3. [Ne II] Fluxes and Upper Limits

We start from the fully reduced VISIR 2.0 spectra, which were corrected for telluric absorption, referenced to the heliocentric frame, and normalized to the continuum. We shift the spectra to the stellocentric reference frame using the stellar radial velocities reported in Table 1. To determine whether the [Ne II] line at 12.81 μm is detected, we calculate the rms per pixel in two spectral regions that are free of emission, shortward and longward of the transition itself. We consider the line to be detected if multiple wavelengths close to 12.81 μm have emission above three times the rms.

Eleven out of the 20 VISIR 2 sources listed in Table 1 have an [Ne II] detection, with HN Tau, V836 Tau, VW Cha, RY Lup, S CrA, and TY CrA being new discoveries[23]—see Figure 1. Note that the bump at $\sim$−65 km s^{-1} in the spectrum of V836 Tau is a spurious feature caused by the removal of high-frequency fringing and of a CO_2 telluric line, while the emission close to the stellar velocity is real. S CrA is a similar spectral type binary separated by 1.″3 (Sullivan et al. 2019), and we detect blueshifted [Ne II] emission of similar intensity from the optically brighter A star and the fainter B star—see Figure 2. Because stellar properties obtained from the optical spectra are for the A+B component (Fang et al. 2018), in the following sections we will use the sum of the [Ne II] emission for this source.

If [Ne II] emission is detected, we follow an approach similar to that adopted for the oxygen forbidden lines in that we fit the minimum number of Gaussian profiles to reproduce the observed line (e.g., Simon et al. 2016; Appendix A).[24] Except for VW Cha, one Gaussian is sufficient to reproduce the observed profiles—see Figure 1. Gaussian FWHMs, centroids (v_c), and EWs for the detected lines are given in Table 2. Uncertainties in v_c and FWHM range from a maximum of 5 km s^{-1} for sources with a low-S/N detection, such as HN Tau and AA Tau, to below 1 km s^{-1} for those with a strong detection, such as SR 21 and TY CrA. However, as the 1σ uncertainty on the stellar radial velocity is typically 1 km s^{-1} (Section 2), even for sources with high-S/N spectra the [Ne II] centroid is not known to better than 1 km s^{-1}.

As with the forbidden oxygen lines (Simon et al. 2016), we call a component HVC (LVC) if the centroid is more (less) blueshifted than 30 km s^{-1}. Following this classification, we would have eight LVCs and six HVCs in our VISIR 2 sample. However, because the HVC (jet emission) centroid is anticorrelated with disk inclination (e.g., Banzatti et al. 2019 for the [O I] λ6300 line), the HVC from highly inclined disks could show blueshifts smaller than 30 km s^{-1} and be classified as LVC, if inclination is not taken into account. We have three

[23] Wa Oph6 has only a tentative 2σ detection at $\sim$−100 km s^{-1}; hence, it is not included among the detections.

[24] We have also tested a different approach whereby we fit a Gaussian profile and calculate the EW in the wavelength range given by the Gaussian centroid $\pm$ 3σ, where σ is the standard deviation of the Gaussian. Due to the poor S/N of the spectra, we found that this method tends to underestimate the EW; hence, we prefer the Gaussian fitting.

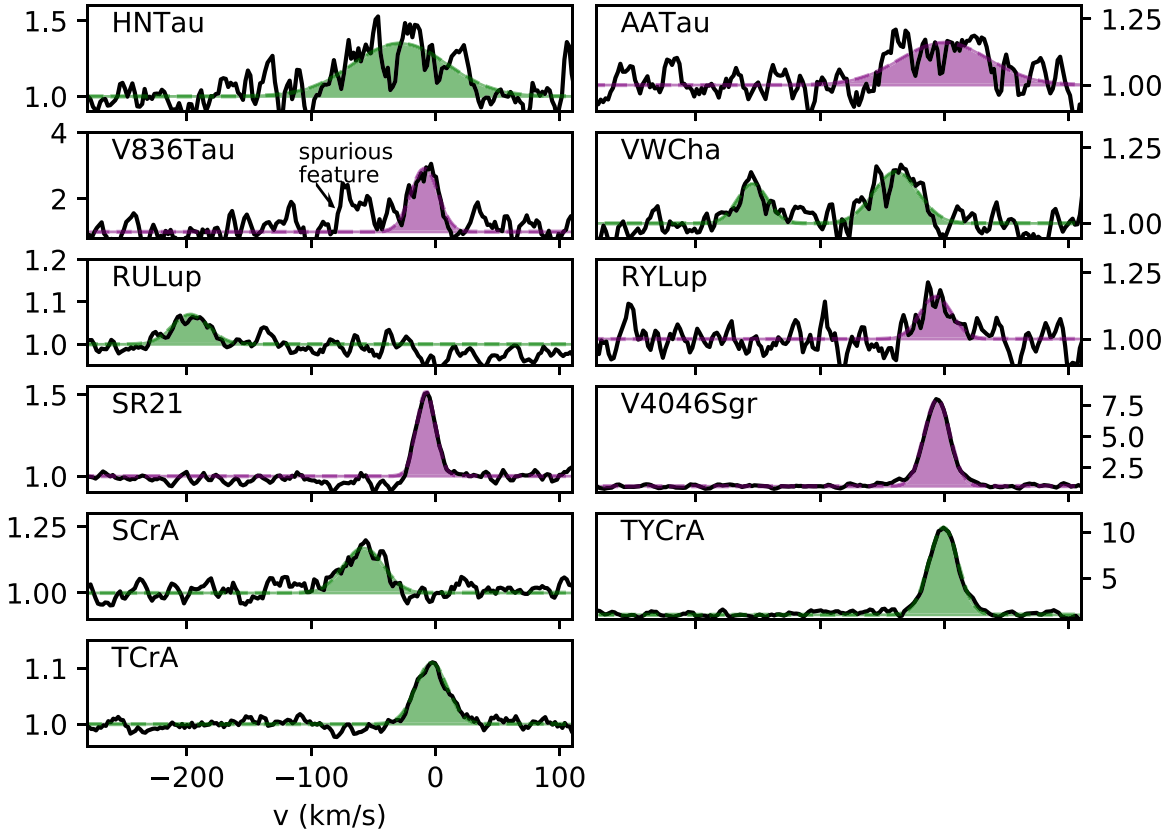

Figure 1. VISIR 2 spectra with an [Ne II] 12.8 μm detection. For visualization purposes, we applied a boxcar smoothing of three velocity elements. For S CrA we show the spectrum from the fainter B component; see Figure 2 for the other component. The best-fit Gaussian profiles are colored in green for the HVC and purple for the LVC following the assignments in Table 2.

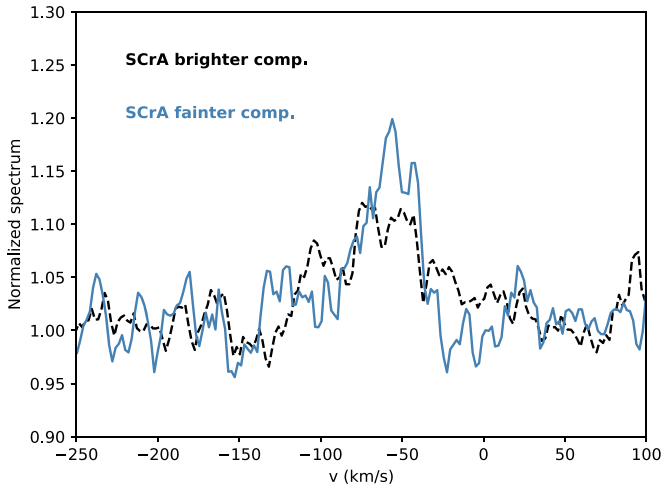

Figure 2. VISIR 2 spectra of the S CrA binary system. Note that for both companions the detected [Ne II] emission is significantly blueshifted from the stellar velocity, here at zero.

such inclined systems in our VISIR 2 sample (Table 2). For HN Tau the reassignment of the [Ne II] LVC into HVC is in line with Fang et al. (2018), who find that even the modestly blueshifted (~ -10 km s^{-1}) optical forbidden line components for HN Tau have line ratios that are more compatible with HVCs than with LVCs. In the case of TY CrA, the low critical density [S II] λ6731 line, which is a well-established jet diagnostic (e.g., Hartigan et al. 1995; Natta et al. 2014), peaks at the stellar velocity (Figure 11). Finally, for T CrA A. Whelan et al. (in preparation) analyze the 2D spectra from several optical forbidden lines and discover a jet aligned with the plane of the sky and thus with radial velocities close to zero. We note that using deprojected velocity centroids and a minimum shock velocity of $\sim$30 km s^{-1} as inferred for several jets (e.g., Hartigan et al. 1994) would result in the same HVC/LVC classification, except for TY CrA. For this complex system (Appendix B), assuming at face value the same inclination of the eclipsing binary as that of the disk would give a deprojected centroid velocity of only -9 km s^{-1}. However, as mentioned above, the detection of the [S II] λ6731 line with no blueshift with respect to the stellar velocity points to a jet in the plane of the sky.

In the absence of [Ne II] emission, we follow Sacco et al. (2012) and provide an upper limit equal to 5 $\times$ rms $\times$ $\sqrt{\mathrm{FWHM}\,\delta v}$, with δv being the line width of a velocity bin ($\sim$2 km s^{-1}) and the FWHM taken to be 20 km s^{-1} for comparison with photoevaporative winds (e.g., Ercolano & Owen 2010). These EW upper limits are given as negative values in Table 2.

To convert EWs into fluxes, we use the flux density near the [Ne II] line measured on low- or medium-resolution Spitzer spectra (e.g., Pontoppidan et al. 2010; Rigliaco et al. 2015). Exceptions are TWA 3A, for which we use WISE/W3 broadband photometry, and T CrA, whose Spitzer flux density at 12.81 μm is twice as large as that measured by VISIR 1 (Sacco et al. 2012), probably due to extended emission within the large slit of Spitzer/IRS. While the absolute flux calibration of the Spitzer spectra is accurate to $\sim$10% (e.g., Pascucci et al. 2007), annual/decadal mid-infrared variability larger than

Table 2
VISIR [Ne II] Detections and Upper Limits

ID	Target	FWHM (km s^{-1})	v_c (km s^{-1})	EW (Å)	i (deg)	F_{cont} (Jy)	Log$L_{[Ne\ II]}$ ($L_\odot$)	Type	i, F_{cont}, [Ne II] References
VISIR 2									
1	GI Tau			−1.59		0.76	<−5.93		1
2	HN Tau[a]	89.03	−28.42	14.05	75	0.95	−4.85	LVC → HVC[b]	2,3
3	AA Tau	83.96	0.01	6.01	59	0.31	−5.7	LVC	4,3
4	DO Tau			−2.24		1.89	<−5.33		3
5	DR Tau			−2.0		1.88	<−5.09		3
6	V836 Tau	25.67	−8.89	22.31	61	0.1	−5.44	LVC	5,3
7	VW Cha	41.83	−39.04	3.3	45	0.73	−5.3	HVC	6,3
7		28.3	−154.38	1.7	45	0.73	−5.59	HVC	3
8	TWA 3A			−2.75		0.89	<−6.73		7
9	GQ Lup			−1.72		0.49	<−5.96		3
10	IM Lup			−1.08		0.48	<−6.13		3
11	RU Lup	33.9	−197.04	1.0	35	4.29	−5.21	HVC	8,3
12	RY Lup	29.68	−6.91	2.12	67	0.76	−5.64	LVC	9,1
13	SR 21[c]	17.44	−7.41	4.14	18	2.1	−5.02	LVC	5,1
14	RNO 90			−0.27		2.05	<−6.36		3
15	Wa Oph6			−0.93		0.82	<−6.18		3
16	V4046 Sgr[c]	24.0	−5.97	76.07	35	0.37	−5.08	LVC	10,1
17	S CrA A	81.97	−60.51	3.71	10	4.61	−4.64	HVC	8,1
17	S CrA B	37.34	−57.83	2.95	10	4.61	−4.74	HVC	1
18	TY CrA	27.26	−0.82	117.65	85	1.5	−3.73	LVC → HVC[b]	11,12
19	T CrA	29.61	−3.11	1.44	90	2.8	−5.26	LVC → HVC[b]	13,14
20	VV CrA			−0.02		27.1	<−6.16		1
VISIR 1									
21	LkCa 15						<−5.41		14
22	TW Hya	16.3	−4.8		7		−5.35	LVC	15,16
23	CS Cha	27.0	−3.3		11		−4.66	LVC	17,18
24	VZ Cha						<−5.58		19
25	T Cha	42.0	−4.0		75		−5.09	LVC	20,18
26	MP Mus	15.9	−4.4		30		−5.48	LVC	21,14
27	Sz 73	60	−99.0		48		−5.08	HVC	22,18
28	Sz 102						<−5.40		18
29	V853 Oph	26.5	−35.8		54		−5.66	HVC	5,19
30	DoAr 44						<−5.7		14
31	RX J1842.9–35						<−5.83		14

Notes. Negative EW values are used to indicate upper limits. Disk inclinations are provided for sources with an [Ne II] detection to evaluate deprojected centroid velocities. References are given for the disk inclination, the continuum flux density (F_{cont}) for VISIR 2 data, and the [Ne II] properties for VISIR 1 data.
[a] Data set acquired on 2017 November 26; the emission is also detected in the 2017 December 28 data set at a slightly lower S/N.
[b] Highly inclined disks; see Section 3 and Appendix B for details on the reassignments.
[c] SR 21 and V4046 Sgr were observed in two and four slit orientations, respectively. The [Ne II] emission is detected in all exposures with similar shape and intensity. Here we provide results from the first exposures, slits oriented N−S.
References. (1) this work (using Spitzer/IRS spectra from either the CASSIS database or from Pontoppidan et al. 2010); (2) Simon et al. 2017; (3) Rigliaco et al. 2015; (4) Loomis et al. 2017; (5) Tripathi et al. 2017; (6) McClure et al. 2015; (7) Kellogg et al. 2017; (8) Pontoppidan et al. 2011; (9) Francis & van der Marel 2020; (10) Rosenfeld et al. 2013; (11) Vaňko et al. 2013; (12) Boersma et al. 2009; (13) E. Whelan et al. 2020, in preparation; (14) Sacco et al. 2012; (15) Andrews et al. 2016; (16) Pascucci et al. 2011; (17) Hendler et al. 2020; (18) Pascucci & Sterzik 2009; (19) Baldovin-Saavedra et al. 2012; (20) Schisano et al. 2009; (21) Kastner et al. 2010; (22) Ansdell et al. 2016.

∼20% is common in young stars (e.g., Espaillat et al. 2011; Kóspál et al. 2012). Therefore, mid-infrared variability, which is mostly unknown for our sources, is likely to be the dominant uncertainty in the [Ne II] luminosities reported in Table 2.

The [Ne II] data for the VISIR 1 sample are collected from the literature and also provided in Table 2 for completeness. We have assigned a classification (Type) to the detections following the work on the forbidden optical lines (Simon et al. 2016).

4. Results

The combined VISIR sample has a total of 17 [Ne II] 12.81 μm detections out of the 31 targets listed in Table 1. Nine sources present an [Ne II] LVC, while eight show an HVC. All disks with an [Ne II] HVC (LVC) detection also have an HVC (LVC) detected in the [O I] λ6300 line. Figure 3 shows the distribution of [Ne II] HVC and LVC detections, as well as nondetections, for the stellar/disk properties summarized in Table 1. When [Ne II] emission is detected, sources with $\dot{M}_{acc} > 10^{-8}\ M_\odot\ yr^{-1}$ have only an HVC. The same is true for systems displaying a large total [O I] λ6300 luminosity ($L_{[O\ I]_{tot}} > 5.4 \times 10^{-5}\ L_\odot$). On the contrary, an [Ne II] LVC is preferentially detected toward sources with low $\dot{M}_{acc}$, low [O I] λ6300 luminosity, and high infrared spectral index ($n_{13-31} > 0.5$).

In the following, we will first explore whether the known correlations between the [O I] luminosities and stellar/disk

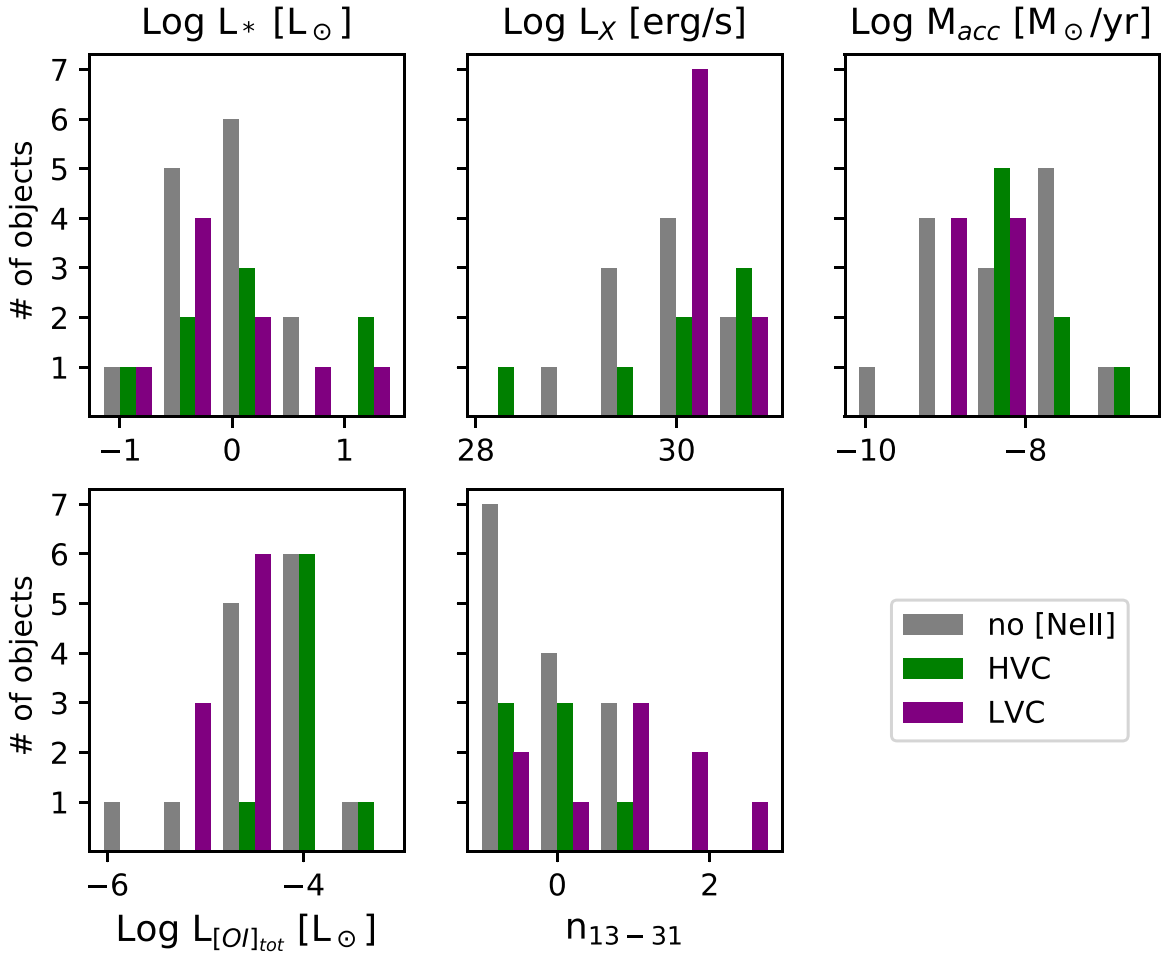

Figure 3. Histograms showing the distribution of [Ne II] HVC (green) and LVC (purple) detections in comparison to that of nondetections (gray) for the sources in Table 1. Note that the total number of objects varies from panel to panel. When [Ne II] emission is detected, HVCs dominate in sources with large $\dot{M}_{\rm acc}$ and large $L_{[\rm O\,I]_{tot}}$, while LVCs dominate in sources with low $\dot{M}_{\rm acc}$, low $L_{[\rm O\,I]_{tot}}$, and large n_{13-31}.

properties apply to the [Ne II] line luminosities (Section 4.1). Next, we will compare the [O I] and [Ne II] line profiles for individual kinematic components to identify possible trends between line centroids and FWHM (Section 4.2).

4.1. Correlations between Line Luminosities and Stellar/Disk Properties

Recent medium- ($\Delta v \sim 35\,{\rm km\,s^{-1}}$) and high-resolution optical ($\Delta v \sim 7\,{\rm km\,s^{-1}}$) surveys have established that there exist a number of correlations between the individual [O I] λ6300 component's properties and stellar and disk properties. In particular, Nisini et al. (2018) showed that the LVC and HVC luminosities correlate better with accretion luminosity and mass accretion rate than with stellar luminosity and mass. Banzatti et al. (2019) further separated LVC into single and double components and discovered that the line EW of single components (without any jet emission) is anticorrelated with the infrared spectral index, i.e., disks with inner dust depletion have lower [O I] λ6300 EWs. In relation to the X-ray luminosity, previous surveys from our group did not identify any correlation between L_X and the $L_{[\rm O\,I]_{LVC}}$ (Rigliaco et al. 2013; Simon et al. 2016). In contrast, McGinnis et al. (2018) reported a positive correlation but found that it was driven by the stronger correlation between the $L_{[\rm O\,I]_{LVC}}$ and L_* in their NGC 2264 sample. The same study reported no correlation between L_X and $L_{[\rm O\,I]_{HVC}}$.

The left panels of Figure 4 show how stellar luminosities (L_*), intrinsic X-ray luminosities (L_X), mass accretion rates ($\dot{M}_{\rm acc}$), and infrared spectral indices (n_{13-31}) relate to the [O I] λ6300 luminosity ($L_{[\rm O\,I]}$) for our combined VISIR sample. We use the `cenken` *R* routine to compute the nonparametric Kendall's τ correlation coefficient and associated probability between the aforementioned stellar/disk properties and the [O I] LVC and HVC luminosities (see Table 3). `cenken` properly accounts for individual upper limits (censored data), which is particularly useful when there are as many nondetections as for the [Ne II] line; see below. For the LVC, we find that our restricted sample recovers the same trends reported in the literature: likely positive correlations between L_* and $\dot{M}_{\rm acc}$ with $L_{[\rm O\,I]_{LVC}}$ (with $\dot{M}_{\rm acc}$ displaying a higher degree of correlation) and a likely negative correlation between n_{13-31} and $L_{[\rm O\,I]_{LVC}}$. For the HVC, our restricted sample only recovers the known correlation between its component [O I] luminosity and $\dot{M}_{\rm acc}$.

In the right panels of Figure 4 we show how the same stellar/disk properties relate to the [Ne II] 12.81 μm luminosities ($L_{[\rm Ne\,II]}$) and test for correlations on the LVC and HVC detections and upper limits (14 over 31) using `cenken` (Table 3). The test only identifies a significant trend between the infrared spectral index and the [Ne II] LVC luminosity: a

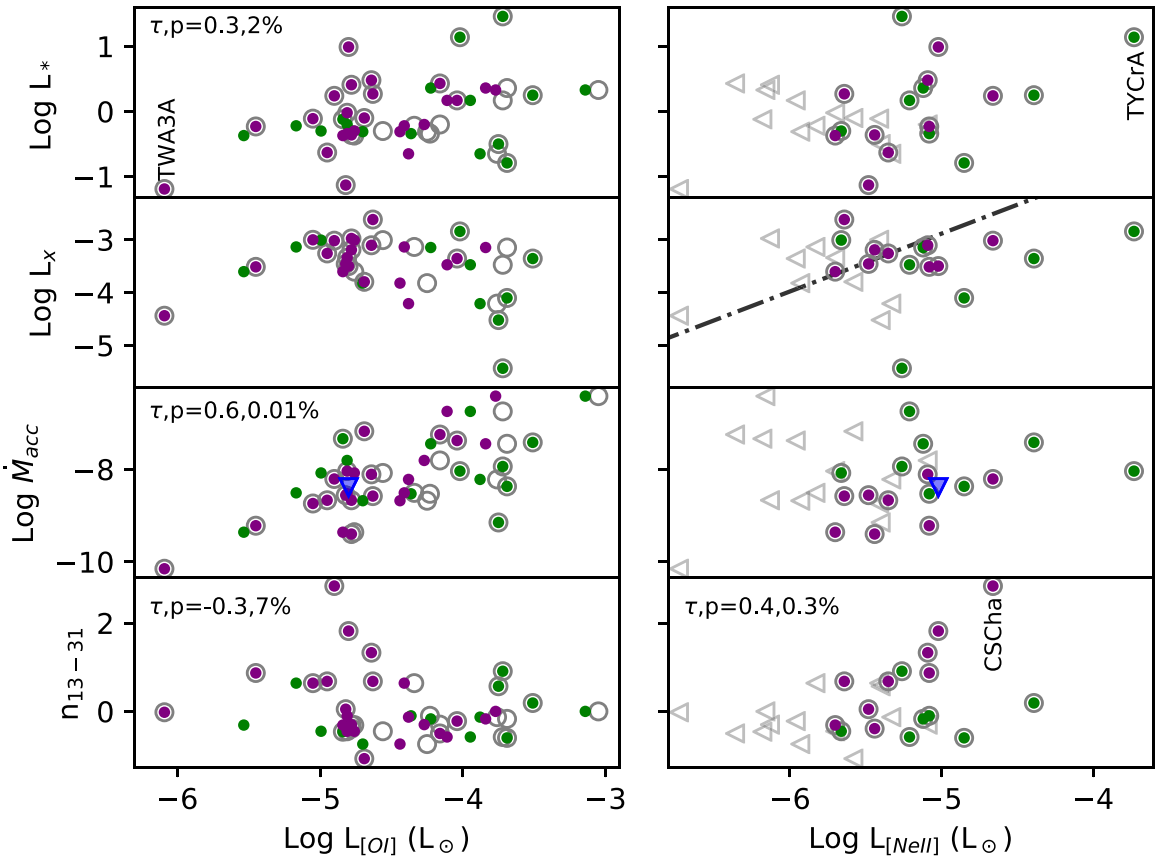

Figure 4. Left panels: stellar luminosity in $L_{\odot}$ (top row), X-ray luminosity in $L_{\odot}$ (second row), mass accretion rate in $M_{\odot}$ yr^{-1} (third row), and infrared spectral index (bottom row) vs. the [O I] λ6300 luminosity; open gray symbols are for the total luminosity, while filled purple (green) symbols are for the LVC (HVC). SR 21, the only source with an upper limit on the mass accretion rate, is plotted with a blue downward-pointing triangle. According to the Kendall's τ test, the LVC [O I] luminosity is likely correlated with the stellar luminosity (positive), mass accretion rate (positive), and spectral index (negative). Right panels: same as the left panels, but for the [Ne II] luminosity. The black dotted–dashed line in the second panel shows the expected relation between X-ray and [Ne II] luminosity (Hollenbach & Gorti 2009). There is a low probability that the infrared spectral index and the [Ne II] LVC luminosity are not positively correlated. Complete statistics for the LVC and HVC are given in Table 3.

Table 3
Summary of the `Cenken` Kendall's τ Tests

Quantity	LVC		HVC	
	$L_{[\mathrm{O\,I}]}$	$L_{[\mathrm{Ne\,II}]}$	$L_{[\mathrm{O\,I}]}$	$L_{[\mathrm{Ne\,II}]}$
L_*	0.3(2)	**0.1(72)**	**0.2(34)**	**0.1(48)**
L_X	**0(81)**	**0.1(38)**	**−0.2(45)**	**0.1(73)**
$\dot{M}_{\rm acc}$	0.6(0.01)	**0(93)**	0.4(6)	**0.1(68)**
n_{13-31}	−0.3(7)	0.4(0.3)	**0.2(32)**	**0(87)**

Note. The first entry (τ) runs from −1 to 1 and indicates the direction of the correlation, while the value in parentheses (p) is the percent probability that the two quantities are uncorrelated. Entries with probabilities larger than 10% are in bold.

low probability that n_{13-31} and $L_{[\mathrm{Ne\,II}]}$ would be so highly correlated through chance alone suggests that disks with inner dust depletion do have higher [Ne II] 12.81 μm LVC luminosities.[25] This trend is not driven by S/N, as exposure times were similar among sources with low and high n_{13-31}. Note that this is opposite to the trend between n_{13-31} and the [O I] LVC luminosity.

To better highlight this result, we show in Figure 5 the ratio of the forbidden line LVC luminosities ($L_{[\mathrm{Ne\,II}]}/L_{[\mathrm{O\,I}]}$) versus the infrared spectral index (n_{13-31}). For the entire VISIR sample, [Ne II] detections (purple circles) and nondetections (purple downward-pointing triangles), the Kendall's τ probability that the two quantities are uncorrelated is only 0.6%. Adding the five Spitzer/IRS sources with no jet emission and whose fluxes would likely be recovered with the narrow slits of VISIR (Appendix C, blue diamonds) further decreases the probability to 0.01%. Except V4046 Sgr (observed with VISIR) and DM Tau (observed with Spitzer), the data suggest that the $L_{[\mathrm{Ne\,II}]}/L_{[\mathrm{O\,I}]}$ ratio increases for $n_{13-31} \geqslant 1.5$, i.e., for more depleted dust cavities, while it is at most ∼0.4 for lower spectral indices. However, note that the majority of the sources with no inner dust depletion, while having strong LVC [O I] emission, are not detected in the [Ne II]. Even when their infrared spectra have an [Ne II] HVC detection and the sensitivity is such to detect an LVC, there is no corresponding LVC [Ne II] detection—see VW Cha and RU Lup. We will further expand on the implications of this finding in Section 5.

4.2. Comparison of Line Profiles

Here we compare the normalized [Ne II] 12.81 μm and [O I] λ6300 line profiles, as well as some of the basic kinematic properties obtained by fitting them with Gaussian profiles. We

[25] Even when excluding CS Cha, which has the highest n_{13-31} and $L_{[\mathrm{Ne\,II}]_{\rm LVC}}$, `cenken` returns a Kendall's τ probability of only 1% that the two quantities are uncorrelated.

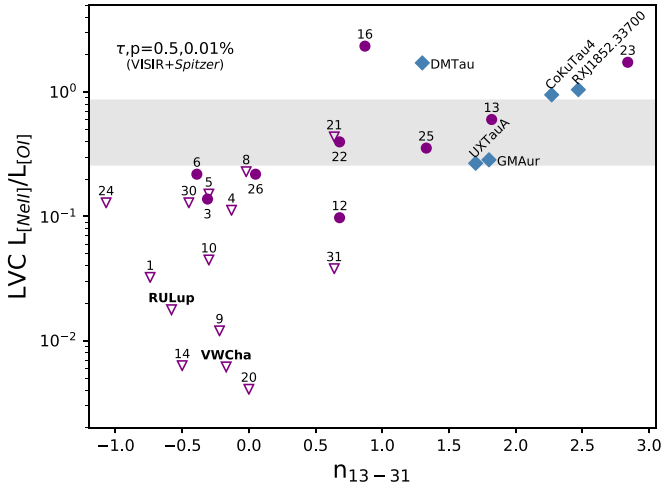

Figure 5. LVC line ratios vs. infrared spectral index. Purple circles and downward-pointing triangles (nondetections) are for the VISIR sample (source ID as in Table 1). RU Lup and VW Cha (in bold) have an HVC but no LVC detection. Blue diamonds are for the Spitzer sources identified in Appendix C. The gray band shows the range of predicted line ratios from Ercolano & Owen (2010), with the upper bound multiplied by a factor of 2 to account for the possible underestimation of the $L_{[\mathrm{Ne\,II}]}$.

discuss AA Tau separately because of the complexity of its inner disk, multicomponent [O I] λ6300 profile, and very large [Ne II] LVC width (Section 4.2.2).

For five out of eight sources, the HVC [Ne II] and [O I] profiles are similar in terms of peak centroids and overall widths (see Figure 6). Exceptions are the profiles from S CrA, RU Lup, and VW Cha. The Kendall's τ probability that the HVC centroids are not correlated with disk inclination is low (1.4% for the [Ne II] and 0.6% for the [O I]). As expected, the HVC centroids from both tracers become less and less blueshifted as we observe disks closer to edge-on, i.e., as the microjet becomes closer to the plane of the sky and the projected radial velocity component toward the observer is reduced. No obvious trend is present between their FWHM and disk inclination (see the Kendall's τ values in the bottom right panel of Figure 6). This is also expected, as the line width of shocked gas traced by the HVC is mostly set by the shock kinematics, hence non-Keplerian (e.g., Hollenbach & McKee 1979; Hartigan et al. 1987). For the [O I] λ6300 lines, Banzatti et al. (2019) reported the same behavior for the HVC centroid and FWHM with disk inclination by analyzing a larger sample of disks.

The LVC behavior is different: [Ne II] velocity centroids are blueshifted even when the [O I] emission is centered at the stellar velocity and the [O I] FWHMs are larger than, or similar to, the [Ne II] FWHMs (Figure 7). There is no obvious trend between the peak centroid of both tracers and disk inclination, while the LVC FWHMs tend to be larger for higher disk inclinations (see the Kendall's τ values in the right panels of Figure 7). The latter trend was already noted for [Ne II] by Sacco et al. (2012) using VISIR 1 data, while for [O I] it was first discussed in Simon et al. (2016) and then revised in Banzatti et al. (2019), where it is shown that single LVC sources present the strongest correlation between the [O I] FWHM and disk inclination. This trend suggests that Keplerian broadening plays some role in setting the LVC line widths. Altogether, this is evidence that the [Ne II] 12.81 μm LVC emission traces predominantly unbound gas from a slow (small blueshifts in the peak centroids), wide-angle (lack of a correlation between centroid and disk inclination) wind. Furthermore, the correlation between FWHM and disk inclination is consistent with a photoevaporative wind or emission close enough to the base of an MHD wind for the gas to retain the Keplerian signature of the launching region. Finally, as the [Ne II] LVC is always more blueshifted than the [O I], the wind traced by [Ne II] originates either at higher elevation or at larger radii than that probed by the [O I] λ6300 line. To gain further insight into which of the two possibilities is the most likely, we turn to the sample of disks with inner dust depletion.

4.2.1. Disks with Dust Inner Cavities or Large Gaps

Figure 7 includes five sources whose spectral energy distribution (SED) hinted early on at significant dust depletion in their inner disk: TW Hya, V4046 Sgr, T Cha, SR 21, and CS Cha—see van der Marel et al. (2016) for a homogeneous analysis. Recently, high-resolution continuum ALMA images have revealed large gaps in the case of TW Hya (~0.5–2 au; Andrews et al. 2016), V4046 Sgr (~4–31 au; Francis & van der Marel 2020), and T Cha (~1–28 au; Hendler et al. 2018), as well as empty cavities of 56, 37, and 69 au for SR 21, CS Cha, and RY Lup, respectively (Francis & van der Marel 2020). Depending on the physical process carving the cavity or gap, its radial extent could be grain size, and hence wavelength, dependent. For instance, dynamical clearing by a planet should lead to large millimeter grains accumulating in pressure maxima beyond the planet location, while small submicron grains are coupled with the gas and can move further in (e.g., Zhu et al. 2012; de Juan Ovelar et al. 2016). This behavior is nicely seen in the disk of T Cha, where the peak emission at 1.6 μm, tracing submicron grains, is several au closer than the peak emission at ALMA wavelengths that trace millimeter grains (Hendler et al. 2018). Whether this behavior is typical to the other disks discussed here is not known.

In relation to the [O I] λ6300 and [Ne II] 12.81 μm line profiles, Pascucci et al. (2011) already noted for TW Hya that while the former is centered at the stellar velocity, the latter is blueshifted. Because submicron dust grains are the main source of opacity, the presence of these grains is necessary to shield redshifted emission from view, to produce a blueshifted line (see photoevaporative wind models with and without cavity in Ercolano & Owen 2010). Based on this fact, and given the decrease in dust extinction with wavelength, Pascucci et al. (2011) concluded that most of the [O I] emission, if tracing a wind, must arise within the dust cavity, while more than 80% of the (blueshifted) [Ne II] emission must arise beyond. In addition, because the small VISIR 1 slit width recovered all the Spitzer/IRS [Ne II] flux, they further constrained its radial extent to within ~10 au from the star.

All other disks with inner cavities or large gaps in Figure 7 display the same behavior in peak centroids. Thus, regardless of the radial extent of the cavity or gap, most of the blueshifted [Ne II] emission must arise beyond the dust cavity or outside the dust gap, sometimes at tens of au, while the [O I] emission, if tracing a wind, is radially confined within the cavity or gap.

It is also possible that the [O I] λ6300 line traces bound disk gas, as proposed for several Herbig Ae/Be systems (e.g., Acke et al. 2005). We follow Simon et al. (2016) in assuming a power-law distribution for the line surface brightness versus

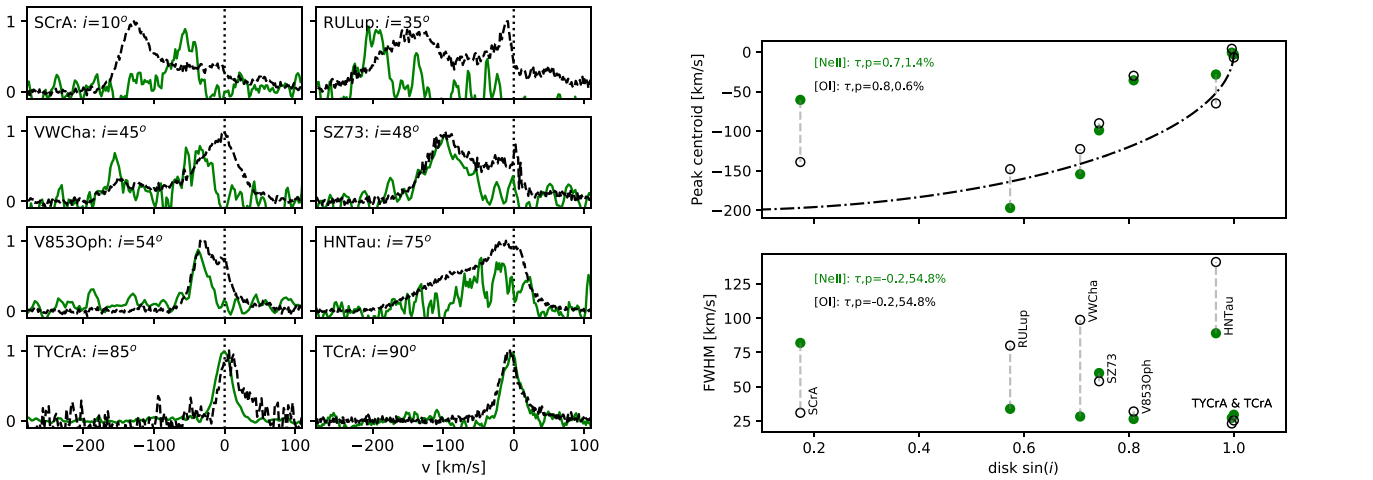

Figure 6. Left panels: comparison of normalized [Ne II] 12.81 μm (green) and [O I] λ6300 (black) profiles for disks with an HVC component. Sources are ordered by increasing disk inclination. Right panels: centroid and FWHM vs. disk inclination. The dotted–dashed line in the top panel shows the projected radial velocity for a microjet with intrinsic velocity of -200 km s^{-1} and perpendicular to the disk midplane.

radial distance from the star ($I_{[\mathrm{O\,I}]} \propto r^{-\alpha}$) and convert it into a velocity profile assuming Keplerian rotation.[26] We then convolve the model line with a velocity width that accounts for instrumental ($\Delta v = 6.6$ km s^{-1}) and thermal broadening at 5000 K as appropriate for collisionally excited gas (Fang et al. 2018). While stellar mass and disk inclination are fixed to the literature values provided in Table 4, we vary the inner and outer radii of the emitting gas and α to find the best fit to the observed line profiles.[27] Using the best-fit surface brightness, we also compute the radius within which 90% of the [O I] emission arises. As shown in Table 4, the inferred power-law indices for the surface brightness span only a small range between 1.5 and 2.5, in agreement with those found by Simon et al. (2016) for disks with dust cavities, and suggest that most of the emission arises close to the star, within less than a few au. Therefore, even in the case of bound disk gas, most of the [O I] λ6300 emission arises closer in than the [Ne II] emission.

4.2.2. AA Tau

AA Tau has long been known to have a peculiar light curve with quasi-cyclic fading episodes at optical wavelengths interpreted as periodic occultations of the star by a warped inner disk (e.g., Bouvier et al. 1999). While the inner disk is thought to be viewed close to edge-on, the outer disk was recently imaged by ALMA and found to be only modestly inclined (59°; Loomis et al. 2017).

As shown in Figure 8, the [O I] λ6300 profile from AA Tau is complex: the HVC (green) is blueshifted by only $\sim$30 km s^{-1}, probably due to the viewing angle, while the LVC (purple) is characterized by a narrow peak and broad wings (Simon et al. 2016; Banzatti et al. 2019). The [Ne II] profile (solid blue), although of much lower S/N, is clearly broader (FWHM $\sim$ 84 km s^{-1}) than the [O I] HVC (FWHM $\sim$ 30 km s^{-1}); it is not as centrally peaked as the [O I] LVC but still fairly symmetric around the stellar velocity. While contamination from HVC emission is possible, the properties of the [Ne II] profile hint at bound disk gas as the dominant emitting region. The same conclusion was reached by Najita et al. (2009), who recovered a broad [Ne II] FWHM of $\sim$70 km s^{-1} in spite of technical issues in retrieving the blue portion of their TEXES spectrum ($R \sim$ 80,000). For comparison, we also show in Figure 8 the normalized stacked 4.7 μm CO rovibrational profile (gray) with the two peaks characteristic of emission from a Keplerian disk. The CO profile is even broader (FWHM = 115 km s^{-1}) than the [Ne II], pointing to a CO-emitting radius of only 0.2 au (Banzatti & Pontoppidan 2015). If [Ne II] at 12.81 μm also traces bound disk gas, it should probe a larger range of disk radii farther out than the CO. A higher-S/N spectrum is necessary to better constrain the [Ne II] emitting region from AA Tau.

5. Discussion

By analyzing a large sample of high-resolution ($\Delta v \sim$ 10 km s^{-1}) mid-infrared spectra, we found that the forbidden [Ne II] line at 12.81 μm, similarly to the [O I] λ6300 line, mostly traces unbound gas flowing away from the star+disk system (see the line centroids v_c in Table 2). Following the kinematic classification applied to optical forbidden lines and by comparing line profiles and basic kinematic properties, we also have evidence for the [Ne II] HVC to originate in fast collimated microjets, while the LVC might trace a slower disk wind.

However, there are also important differences between these two tracers. First, while the [O I] HVCs are typically accompanied by LVCs (Banzatti et al. 2019), the [Ne II] detections show either an HVC or an LVC, with about an equal number of the two components in these spectra (Table 2). Second, while the $L_{[\mathrm{O\,I}]_{\mathrm{LVC}}}$ decreases as the dust inner disk is depleted (higher n_{13-31} index), the $L_{[\mathrm{Ne\,II}]_{\mathrm{LVC}}}$ increases (Figure 4, bottom panels). Finally, while most HVCs have similar morphologies in the two forbidden lines (Figure 6), the [Ne II] LVC profiles, most of which are for systems with dust-depleted inner disks, are typically more blueshifted than the [O I] LVC (Figure 7). Interestingly, even disks with tens of au, millimeter dust cavities like SR 21 or CS Cha present blueshifted [Ne II] emission pointing to slow winds outside the gravitational radius (e.g., Equation (2) in Alexander et al. 2014). In contrast, their [O I] emission is centered at the stellar radial velocity and could thus arise from bound disk gas (Table 4) or a wind inside the dust cavity, as already discussed for TW Hya (Pascucci et al. 2011). Thus, by combining the [O I] and [Ne II] diagnostics, we

[26] Routine keprot.pro by Acke et al. (2005).

[27] Using the IDL routine *mpfitfun* with uncertainties on the flux equal to the rms on the continuum next to the line.

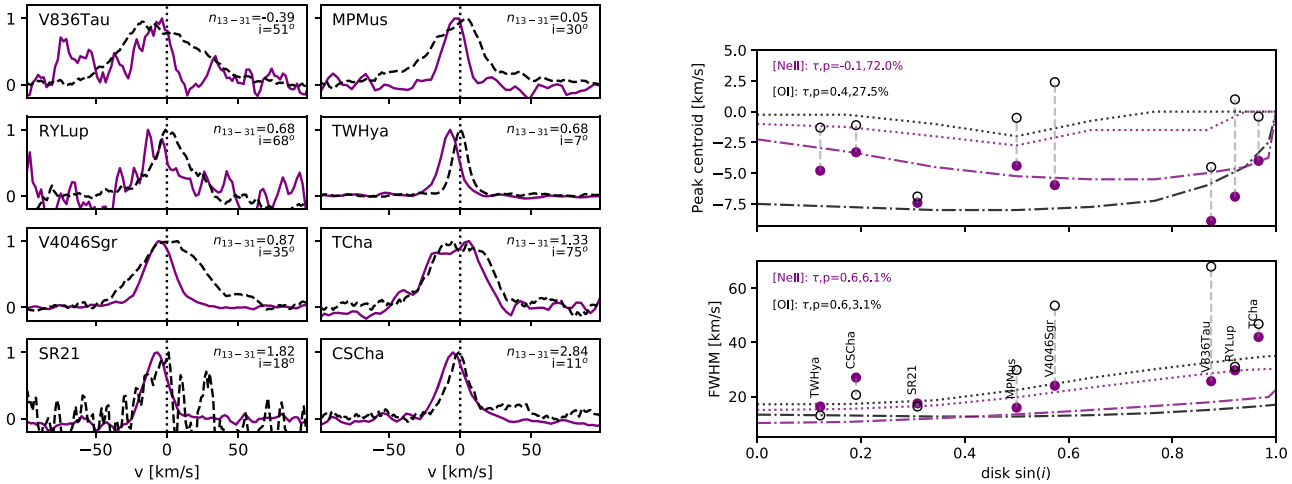

Figure 7. Same as Figure 6, but for the LVC, [Ne II] in purple. Left panels: sources are ordered by increasing infrared spectral index (n_{13-31}). The disk inclination (i) is also provided for each target. Right panels: dotted–dashed and dotted lines are predictions from the Ercolano & Owen (2010) photoevaporative models with log (L_X) = 30.3 erg s^{-1} for full disks and disks with an 8.3 au hole in the gas and dust, respectively (purple lines for the [Ne II] 12.81 μm, black lines for the [O I] λ6300 transition).

Table 4
Keplerian Modeling for the [O I] λ6300 Profiles of Disks with Inner Cavities or Large Gaps: Input and Best-fit Parameters

Target	M_* ($M_\odot$)	i (deg)	M_* Ref.	$R_{\rm in}$ (au)	$R_{90\%}$ (au)	α
RY Lup	1.4	67	1	0.29	2.3	2.1
TW Hya	0.6	7	3	0.06	0.4	2.2
V4046 Sgr	1.8	35	4	0.27	1.2	2.5
T Cha	1.5	75	5	0.15	2.9	1.5
SR 21	1.8	18	3	0.08	0.8	1.9
CS Cha	1.3	11	6	0.02	0.17	2.1

References. (1) Hendler et al. 2020; (3) Fang et al. 2018; (4) Rosenfeld et al. 2013; (5) Schisano et al. 2009; (6) Pascucci et al. 2016. References for disk inclinations are given in Table 2.

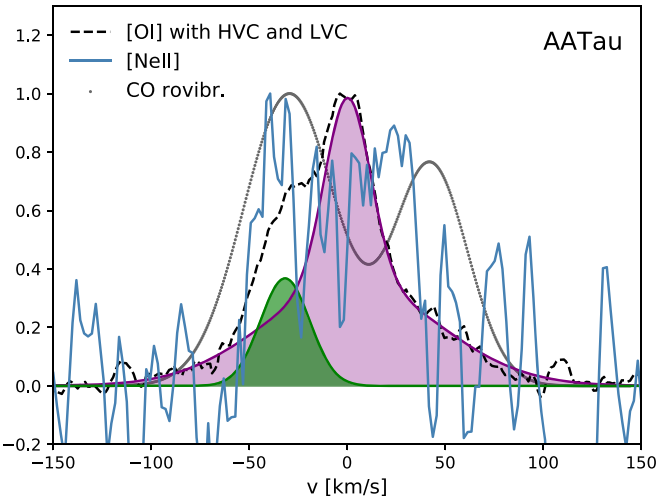

Figure 8. Comparison of line profiles for AA Tau in the stellocentric reference frame: [O I] λ6300 (black dashed line) with HVC (green) and LVC (purple) decomposition (Banzatti et al. 2019); [Ne II] 12.81 μm emission (blue solid line; this work); stacked CO rovibrational profile at 4.7 μm (gray dots; Banzatti & Pontoppidan 2015).

find evidence of slow flows, possibly disk winds, at all disk evolutionary stages.

In the following, we will discuss the ionization of Ne atoms and how our observations compare with predictions from static disk and wind models (Sections 5.1 and 5.2). As none of the current models can fit the entirety of the data at hand, we also sketch an evolutionary scenario that might explain the existing data (Section 5.3).

5.1. Static Disk Models and Ionization of Ne Atoms

Hollenbach & Gorti (2009) pointed out that if one considers reasonable EUV and X-ray spectra for young stars, the X-ray-heated disk layer produces more [Ne II] 12.81 μm emission than the EUV-heated layer because in the latter most photons are used to ionize H rather than Ne (see also Glassgold et al. 2007; Ercolano & Owen 2010; Aresu et al. 2012). Observations also suggest that the [Ne II] emission mostly traces an X-ray rather than an EUV layer. If the EUV luminosity scales with ν^{-1}, as suggested by the fact that νL_ν in the FUV is about the same as in the X-ray, the [Ne III] 15.5 μm luminosity should be higher than the [Ne II] at 12.81 μm in the EUV-heated layer (Figure 1 in Hollenbach & Gorti 2009). However, the [Ne III] 15.5 μm line is rarely detected in Spitzer/IRS spectra, and, when detected, the [Ne III]-to-[Ne II] line flux ratios are significantly less than 1, except for SZ Cha, where the ratio is close to unity (e.g., Najita et al. 2010; Szulágyi et al. 2012; Espaillat et al. 2013). Regardless of the EUV spectrum, centimetric radio data demonstrate that the EUV luminosity impinging on the disk surface is too low to reproduce the observed [Ne II] 12.81 μm luminosities (Pascucci et al. 2014). This means that Ne atoms are ionized by 1 keV hard X-ray photons via the Auger effect. X-rays are also likely to heat the gas in the same region, although it remains unclear whether they are the dominant heating source.

A prediction from static disk models is that the [Ne II] 12.81 μm luminosity should scale almost linearly with L_X in the X-ray-heated disk layer (e.g., Hollenbach & Gorti 2009; Aresu et al. 2012). While several of the data points fall on the predicted relation (see Figure 4), the current data set cannot confirm the existence of a correlation between $L_{\rm [Ne\,II]}$ and L_X. On the one hand, it would be important to expand the sample to cover a broader range of [Ne II] and L_X luminosities. On the

other hand, it would be interesting to test whether the predicted $L_{[\mathrm{Ne\,II}]}$–L_X correlation for a static atmosphere holds also in a flowing one (e.g., Ercolano & Owen 2010), as the data demonstrate that the [Ne II] 12.81 μm line mostly traces unbound gas (Section 4.2).

5.2. Photoevaporative and MHD Disk wind Models

As summarized in the Introduction, significant progress has been made recently in understanding the origin of optical forbidden lines, such as [O I] λ6300. In particular, there is consensus on its HVC primarily tracing a microjet and its LVC-BC tracing an inner MHD wind (e.g., Ray et al. 2007; Simon et al. 2016; McGinnis et al. 2018; Weber et al. 2020). Uncertainty remains on the LVC-NC, which is attributed either to some other region in the inner MHD wind (e.g., Banzatti et al. 2019) or to an outer photoevaporative wind (e.g., Weber et al. 2020).

For the [Ne II] 12.81 μm line investigated here, the spectral resolution and sensitivity do not allow us to further decompose identified LVCs into BC and NC. Hence, we can only treat the entire [Ne II] LVC as a single phenomenon. We will examine our results in the context of photoevaporative models and then move on to recent analytic MHD disk wind models.

In relation to photoevaporative X-EUV models, Ercolano & Owen (2010) find that disks with an inner hole in the dust and gas produce a factor of $\sim$2 higher $L_{[\mathrm{Ne\,II}]}$ than full disks, mostly because stellar X-rays are not absorbed by the inner disk and can thus heat and ionize a larger/farther away portion of the wind. This trend agrees with our finding that the $L_{[\mathrm{Ne\,II}]_{\mathrm{LVC}}}$ is higher for sources with dust-depleted inner disks (Figure 4 bottom right panel). However, the predicted [Ne II]-to-[O I] line ratios are rather similar (gray horizontal band in Figure 5) and cannot explain the majority of our data, including the many stringent LVC upper limits (downward-pointing triangles). In addition, because the predicted [O I] λ6300 line is extremely sensitive to high temperatures ($E_{\mathrm{up}} \sim 22{,}830$ K), it probes the hot inner portion of the wind closer to the star than the [Ne II] line; hence, the [O I] profiles are more blueshifted than the [Ne II] for full disks, or both mostly at the stellar velocity for disks with holes (see Figure 7, as well as Picogna et al. 2019). Both of these trends are opposite to what is observed.

Ballabio et al. (2020) used the self-similar solutions for thermal disk winds developed by Clarke & Alexander (2016) to calculate [O I] and [Ne II] line profiles for different disk inclinations. For a given sound speed and the same disk inclination, the models predict similar blueshifts for the [Ne II] and [O I] lines, while the [O I] FWHM tends to be larger than the [Ne II]. When compared with previous data drawn from the literature, the model for a 10 km s^{-1} thermal wind successfully reproduces the blueshifts and widths of the observed [Ne II] LVC lines. The observed [O I] line blueshifts favor cooler low-velocity gas models (c_s = 3–5 km s^{-1}), but the predicted widths for these models are less than 15 km s^{-1}, much smaller than the observed ones. This suggests that a single thermal wind model cannot easily reproduce the observations of both [Ne II] and [O I] λ6300 LVC lines.

Recently, Weber et al. (2020) computed line profiles from an X-ray photoevaporative wind model based on the radiation-hydrodynamical calculations of Picogna et al. (2019) and an analytic MHD wind model following Blandford & Payne (1982), with photoionization as in Ercolano & Owen (2010). Although they do not discuss the [Ne II] 12.81 μm emission, they cover several optical forbidden lines, including [O I] λ6300. As in their MHD models the high critical density [S II] λ4068, [O I] λ5577, and [O I] λ6300 lines come from within a few au and close to the disk surface, the synthetic profiles have Keplerian double peaks[28] for disks inclined by more than 30°, which are not observed (e.g., Banzatti et al. 2019). They conclude that if the MHD wind (producing the HVC and BC) is also accompanied by a photoevaporative wind, then the Keplerian trough in the BC can be filled by the narrow component emission from the thermal wind. Our major concern with the addition of such a photoevaporative wind is in its radially and vertically extended lower-density region that is bright in the [S II] λ6730 line (Figure 1 in Weber et al. 2020). The predicted [S II] λ6730 line luminosities are similar to, or higher than, the [O I] λ6300 luminosities, and the mean [S II] λ6730 over λ4068 line ratio for models with accretion luminosity comparable to the observed ones ($L_{\mathrm{acc}} = 3 \times 10^{-2}\,L_{\odot}$) is slightly above unity. On the contrary, observations show that the [S II] λ6730 line is far less common than the [O I] λ6300 line or the [S II] λ4068 line; when detected it is usually as an HVC, not an LVC, and, combining contemporaneous LVC detections and nondetections, the mean [S II] λ6730 over λ4068 line ratio is $\sim$0.15, well below unity (e.g., Hartigan et al. 1995; Pascucci et al. 2011; Natta et al. 2014; Simon et al. 2016; Fang et al. 2018).

As MHD wind models have a less extended low-density region (Weber et al. 2020), and considering the empirical correlations between the [O I] HVC and its LVB-BC and NC (Banzatti et al. 2019), we lean toward prior interpretations that attribute the optical forbidden lines solely to an MHD wind and a jet in systems with full disks and high accretion rates (e.g., Natta et al. 2014; Fang et al. 2018; Nisini et al. 2018; Banzatti et al. 2019).

5.3. An Evolutionary Sketch for Disk Winds

Given that none of the current models exactly fit the observations at hand (Section 5.2), we put forth an empirically motivated evolutionary scenario that can be tested by future observations and disk wind models.

One of the most important results from our study is that the majority (9/11) of full disks, i.e., disks with $n_{13\text{–}31} < 0$, have an inner MHD disk wind identified via the [O I] λ6300 LVC emission but lack an [Ne II] 12.8 μm LVC detection (Figure 5). As shown in Figure 5 and Table 2, 3σ $L_{[\mathrm{Ne\,II}]}$ upper limits, calculated for an FWHM that is appropriate for an LVC, are stringent enough for most sources and suggest that the [Ne II] LVC in full disks is several times weaker than in disks with inner dust depletion, while the reverse is true for [O I] λ6300 (whose emission diminishes in disks with larger dust cavities). These results strongly suggest that hard X-ray photons ionizing Ne atoms are somehow screened in full disks and do not pass beyond the inner wind, where they would produce enough detectable [Ne II] emission as shown, e.g., in the fully atomic photoevaporative models of Ercolano & Owen (2010, see their Figure 3).

Hollenbach & Gorti (2009) discussed the penetration of high-energy stellar photons through inner winds, which they modeled following the "X wind" prescription (Shu et al. 1994).

[28] Note that line profiles from MHD wind models are very sensitive to the assumed, and not well-constrained, structure of the flow (see, e.g., the different forbidden line profiles in Garcia et al. 2001; Shang et al. 2010).

As such, these inner winds arise within 10 stellar radii where all dust has likely sublimated. They find that a gas column density of $\sim 10^{22}$ cm^{-2} is required for 1 keV optical depth of unity, which translates into a wind mass-loss rate less than $\sim 4 \times 10^{-8}\, M_{\odot}\, \mathrm{yr}^{-1}$ for hard X-rays to penetrate the wind. Interestingly, this value is within a factor of a few of the mass accretion rate below which [Ne II] LVC detections dominate (Figures 3 and 4). Soft X-rays peaking at $\sim$0.2 keV are screened by a column of only $\sim 10^{20}$ cm^{-2}; hence, they are mostly absorbed at the surface of the wind exposed to the star: this behavior is seen in the models of Ercolano & Owen (2010) through the [O I] λ6300 line, which mostly traces soft X-rays. But different penetration depths alone are unlikely to explain the ensemble of the observations. The excitation temperature of the [Ne II] line is only $\sim$1100 K, and therefore the gas would have to be cooler than a few $\times$ 10^2 K to not excite the transition; fully atomic gas cannot typically cool efficiently (e.g., Ercolano et al. 2008). However, if the portion of the inner wind where hard X-rays are absorbed is mostly molecular, efficient cooling (e.g., Gorti et al. 2016) could suppress the [Ne II] emission below detectable values.

Figure 9 sketches a possible evolutionary scenario. The top panel illustrates a typical full, flared disk with an inner MHD wind that is mostly atomic out to a radial distance where soft X-rays penetrate. This hot (>5000 K) atomic layer, perhaps heated also by ambipolar diffusion (e.g., Safier 1993), would be responsible for the [O I] λ6300 LVC. Hard X-rays penetrate deeper in the wind and would be absorbed in a mostly molecular layer that is too cool to produce detectable [Ne II] emission. The narrow component (FWHM = 10–50 km s^{-1}) of the CO fundamental emission is found to trace gas of 200–700 K (e.g., Banzatti & Pontoppidan 2015) and hence might trace this cooler molecular wind. Interestingly, RU Lup and S CrA, two of our disks that have [O I] HVC and LVC emission but only an [Ne II] HVC component (see Figure 6), present astrometric signals in their CO fundamental lines that are consistent with a molecular wind (Pontoppidan et al. 2011).

The bottom panel of Figure 9 illustrates a typical disk with a dust inner cavity, lower accretion, and weaker inner wind. At this stage X-ray photons penetrate deeper. The [O I] LVC emission, which is correlated with mass accretion rate (Figure 4), weakens and could trace larger radii, as suggested by the positive correlation between FWHM and spectral index (Banzatti et al. 2019). Still, most of the emission would arise within the dust cavity (Section 4.2.1). The molecular layer is also significantly reduced, which is supported by the finding that nearly all disks with dust-depleted inner cavities show no evidence for infrared water emission lines in their Spitzer/IRS spectra and CO-emitting radii are larger (Salyk et al. 2015; Banzatti et al. 2017). The hard 1 keV X-ray photons would pass through the inner wind and reach the edge of the dust cavity where the disk starts flaring: there, they would ionize Ne atoms and produce detectable [Ne II] 12.81 μm emission in an outer wind. As discussed in Section 4.2, the lack of correlation between [Ne II] LVC centroid and disk inclination suggests that this outer wind has a wide opening angle. However, current data are not sufficient to establish whether the wind is photoevaporative or MHD in nature and its presence does not imply that the dust cavity is opened by the wind.

Recently Simon et al. (2018) put forward a preliminary model to reconcile largely laminar MHD winds, which produce significant turbulent velocities in the outer disk, and the limits on turbulent broadening obtained with ALMA. A key component of this model is a massive wind inside 30 au that would block high-energy stellar photons, in particular X-rays and FUV photons. While our data do not constrain the screening of FUV photons, they provide some evidence for the inner region of full disks blocking X-rays and not reaching the outer disk.

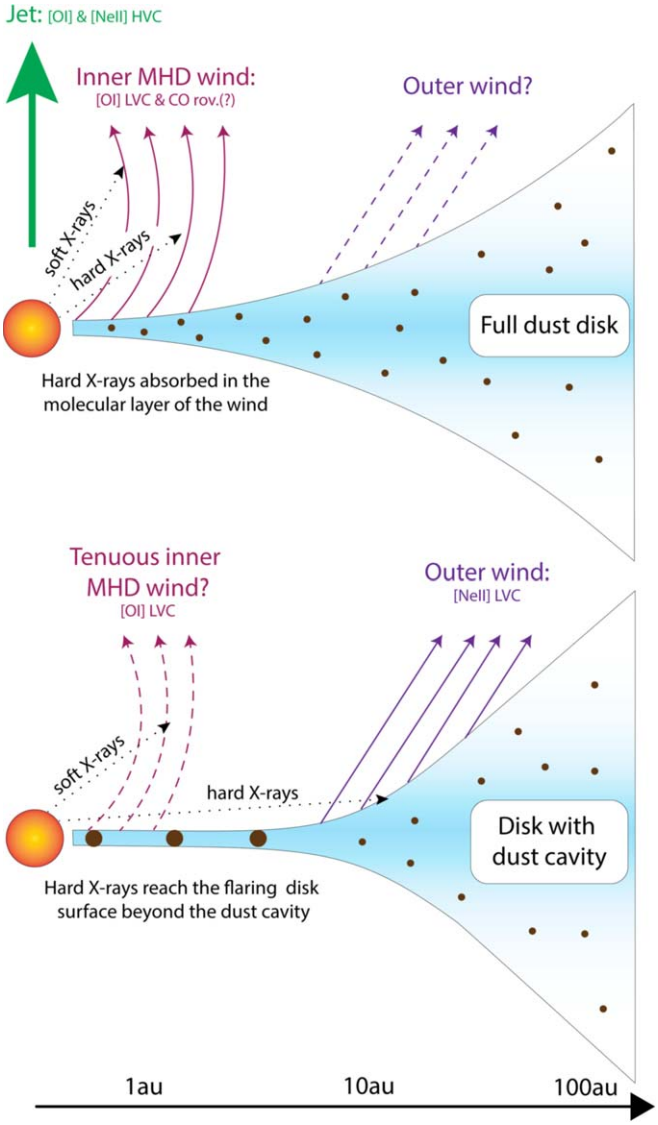

Figure 9. Evolutionary sketch. Top panel: full dust disk with an inner MHD wind that screens X-ray photons. Bottom panel: disk with dust cavity and a tenuous inner wind that enables hard X-ray photons to penetrate deeper and produce detectable [Ne II] LVC emission. The source in the top panel is a higher accretor than the one in the bottom panel and powers a jet detected as HVC.

6. Summary

We have analyzed a sample of 31 disks that were observed with high-resolution optical ($\Delta v \sim 7$ km s^{-1}) and infrared ($\Delta v \sim 10$ km s^{-1}) spectra covering the [O I] λ6300 and the [Ne II] 12.81 μm lines. Our VISIR 2 infrared survey discovered six new [Ne II] detections and confirmed five detections previously reported in the literature. Following analysis carried out at optical wavelengths (e.g., Simon et al. 2016), we fit the detected lines with Gaussian profiles and classified them into

HVC (or LVC) depending on whether the line centroid is more (or less) blueshifted than 30 km s^{-1} from the stellar radial velocity. Combining the VISIR 2 and literature VISIR 1 results, we explored whether the known correlations between the [O I] luminosities and stellar/disk properties apply to the [Ne II] luminosities. In addition, we compared the detected [Ne II] 12.81 μm and [O I] λ6300 profiles to investigate whether these transitions trace the same region. Our main results can be summarized as follows:

1. All 17 sources with [Ne II] detections present either an HVC or an LVC, in about equal numbers. This is very different from the [O I] λ6300, where the LVC is found in most sources, many of which also have an HVC (Banzatti et al. 2019).
2. High accretors ($\dot{M}_{\rm acc} > 10^{-8}\,M_{\odot}\,{\rm yr}^{-1}$) with [Ne II] detections present only an HVC in this line. [Ne II] LVCs are preferentially detected in sources with low $\dot{M}_{\rm acc}$, low [O I] λ6300 emission, and high infrared spectral index (n_{13-31}).
3. The [Ne II] and [O I] luminosities display the opposite behavior with n_{13-31}: while the $L_{[\rm O\ I]_{LVC}}$ decreases as the dust inner disk is depleted (higher n_{13-31} index), the $L_{[\rm Ne\ II]_{LVC}}$ increases.
4. The [Ne II] and [O I] HVC profiles are generally similar, with centroids and FWHMs showing the expected behavior from shocked gas in microjets, i.e., centroids less blueshifted for closer-to-edge-on disks and FWHMs independent of disk inclination.
5. The [Ne II] LVC profiles are more blueshifted and typically narrower than the [O I] LVC profiles. Both FWHMs increase for closer-to-edge-on disks, while the peak centroids are independent of disk inclination. This is evidence that the [Ne II] LVC predominantly traces unbound gas from a slow, wide-angle wind that has not completely lost the Keplerian signature from its launching region.

As the majority of full disks in our survey have an inner MHD disk wind detected via the [O I] LVC but lack an [Ne II] LVC, we infer that the ~1 keV hard X-ray photons needed to ionize Ne atoms are somehow screened in full disks. We suggest that this screening occurs in inner MHD disk winds that, except for a hot surface exposed to the star and likely traced via the [O I] LVC, are mostly molecular. The molecular wind, suggested in a few sources via CO spectroastrometry (Pontoppidan et al. 2011), would absorb most of the hard X-rays and, thanks to efficient cooling, produce little [Ne II] emission, below the VISIR sensitivity. As the dust inner disk is depleted and the inner wind and accretion weaken, hard X-rays can penetrate deeper, reaching the outer edge of the dust cavity where the gas disk flares. There, they would heat and ionize a larger surface area that becomes detectable in our survey via the [Ne II] 12.81 μm line. At the same time, the [O I] λ6300 luminosity, which strongly correlates with $\dot{M}_{\rm acc}$, diminishes and, being confined within the dust cavity, can lose the kinematic signature of a wind. JWST/MIRI observations of selected disks with large dust cavities, like SR 21 and RY Lup, could spatially resolve the outer wind in the [Ne II] 12.81 μm line.

Recently, Fang et al. (2018) used a combination of optical forbidden lines from atomic and ionic species to estimate the LVC wind mass-loss rates. If our evolutionary sketch is correct and the inner MHD winds from full disks have a significant molecular component, the Fang et al. (2018) values should be taken as lower limits. Expanding the set of molecular diagnostics for the inner winds, as well as the sample of disks with detections, to date restricted to suggestive evidence only in a handful of disks, will be important to better constrain wind mass-loss rates. Disk wind models that properly couple thermodynamics and hydrodynamics are being developed (e.g., Gressel et al. 2020) and are necessary to test our proposed evolutionary scenario.

This work is based on observations collected at the European Southern Observatory under ESO program 198.C-0104. I.P., U. G., and S.E. acknowledge support from a Collaborative NSF Astronomy & Astrophysics Research grant (ID: 1715022, ID:1713780, and ID:1714229). This material is based on work supported by the National Aeronautics and Space Administration under agreement No. NNX15AD94G for the program *Earths in Other Solar Systems*. The results reported herein benefited from collaborations and/or information exchange within NASA's Nexus for Exoplanet System Science (NExSS) research coordination network sponsored by NASA's Science Mission Directorate. R.D.A., G.B., and C.H. acknowledge funding from the European Research Council (ERC) under the European Union's Horizon 2020 research and innovation program (grant agreement No. 681601). G.B. acknowledges support from the University of Leicester through a College of Science and Engineering PhD studentship. C.H. is a Winton Fellow, and this research has been supported by Winton Philanthropies/The David and Claudia Harding Foundation. This project has been carried out as part of the European Union's Horizon 2020 research and innovation program under the Marie Skłodowska-Curie grant agreement No. 823823 (DUSTBUSTERS).

Facility: ESO(VISIR).

Software: `astropy` (The Astropy Collaboration et al. 2013, 2018), `mpfitfun` (MINPACK-1 in Jorge Moré & Stephen Wright 1987), `cenken` (Helsel 2005 and Akritas et al. 1995).

Appendix A
Reduction of Unpublished Optical Spectra and [O I] Line Luminosities

The sources CS Cha, MP Mus, T Cha, TY CrA, T CrA, V4046 Sgr, and VW Cha have very noisy or no published high-resolution optical spectra. For all of them except TY CrA, we retrieved from the ESO archive[29] the highest-S/N UVES spectra ($R \sim 45{,}000$) available.[30] For TY CrA we used an unpublished Magellan/MIKE spectrum at a similar spectral resolution ($R \sim 42{,}000$). The data reduction was carried out as in Fang et al. (2018) and Banzatti et al. (2019) and includes removal of telluric absorption lines and photospheric features, as well as subtraction of the stellar radial velocity, to bring the spectra in the stellocentric reference frame. The stellar radial velocities for all sources except TY CrA and V4046 Sgr are derived by cross-correlating each star optical spectrum with the synthetic spectrum of a star that has the same effective temperature (see Table 1). For TY CrA and V4046 Sgr we use the center-of-mass radial velocity of the eclipsing binary and that of the circumbinary CO disk, respectively; see further details in Appendix B. Figure 10 shows the seven archival

[29] http://archive.eso.org/cms.html

[30] In the case of V4046 Sgr we combine six UVES spectra to increase the S/N.

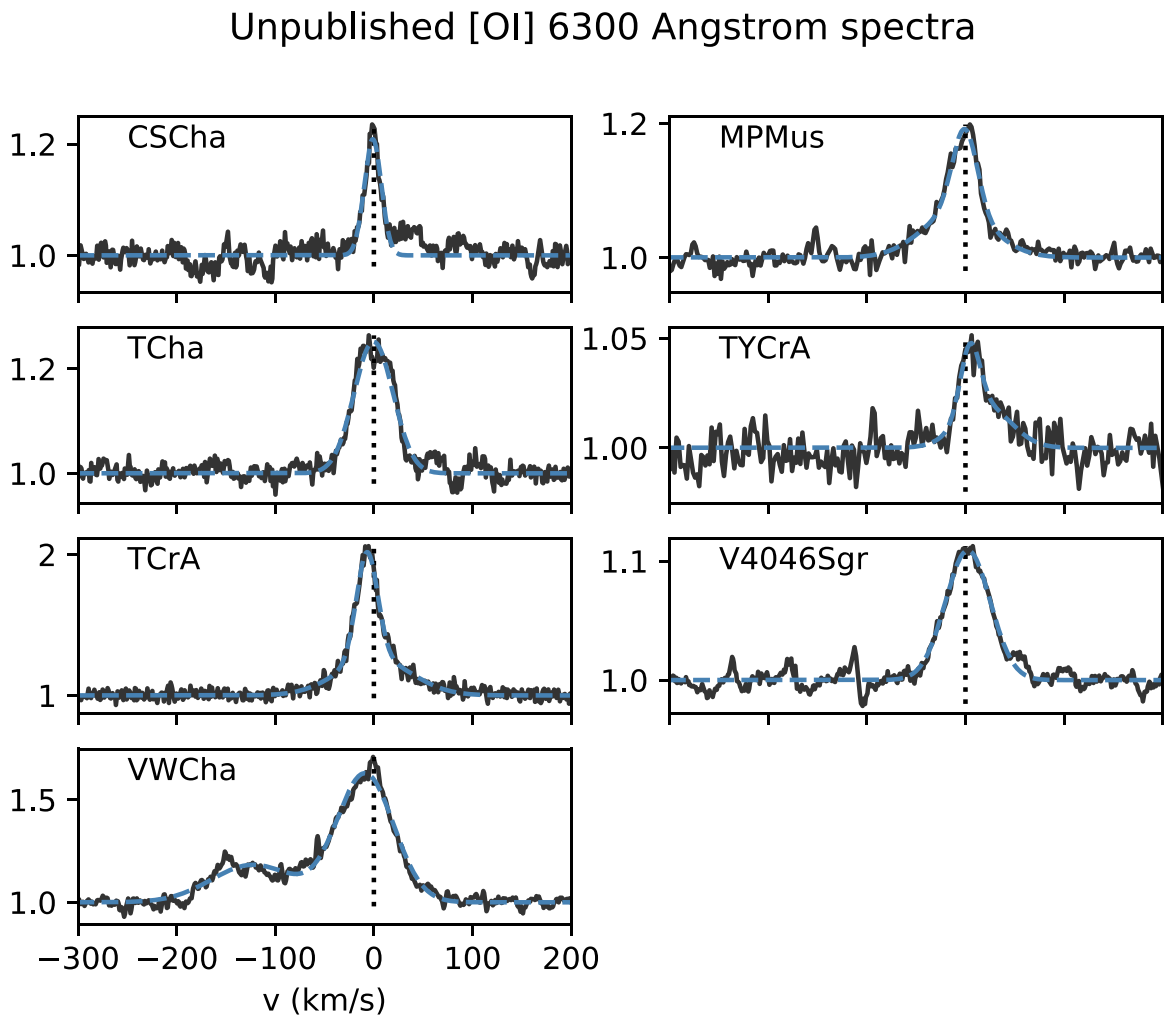

Figure 10. Unpublished VLT/UVES and MIKE/Magellan spectra utilized in this work showing the [O I] λ6300 emission in the stellocentric reference frame. The blue dashed line in each panel shows the best fit using the Gaussian components in Table 5.

Table 5
[O I] λ6300 Decomposition from Unpublished High-resolution Spectra

Target	FWHM (km s^{-1})	v_c (km s^{-1})	EW (Å)	Type	V	A_V	V, A_V Ref.	Log $L_{[O\,I]}$ ($L_\odot$)
CS Cha	20.6	−1.1	0.1	LVC-NC	11.7	0.8	1	−4.9
MP Mus	29.8	−0.5	0.08	LVC-NC	10.44	0.17	2	−5.21
	82.8	−8.6	0.13	LVC-BC				−5.04
T Cha	46.8	−0.4	0.26	LVC-BC	11.6	1.3	3	−4.64
TY CrA	23.2	4.6	0.02	LVC → HVC[a]	9.26	1.98	4	−4.44
	61.8	19.3	0.03	LVC → HVC[a]				−4.23
T CrA	25.4	−7.0	0.43	LVC → HVC[a]	12.04	1.9	5	−4.06
	87.9	0.4	0.51	LVC → HVC[a]				−3.99
V4046 Sgr	53.6	2.4	0.13	LVC-BC	10.68	0.0	6	−5.45
VW Cha	67.7	−8.8	0.95	LVC-BC	12.8	1.9	7	−3.84
	98.8	−122.6	0.4	HVC				−4.21

Notes. The V magnitude of T Cha varies by up to 1.5 mag; we report here its median value.
[a] The 2D spectrum of T CrA reveals a jet close to the plane of the sky; hence, it is not possible to distinguish the jet emission from any LVC (A. Whelan et al. 2020, in preparation). The disk around the quartenary star system TY CrA is likely seen edge-on; hence, any jet emission will be close to the plane of the sky. Our assignment is corroborated by the [S II] λ6731 detection, which is sensitive to jet emission and peaks very close to the [O I] λ6300 lowest-velocity component.
References. (1) Espaillat et al. 2007; (2) Mamajek et al. 2002; (3) Schisano et al. 2009; (4) Vioque et al. 2018; (5) Garcia Lopez et al. 2006; (6) Donati et al. 2011; (7) Manara et al. 2017.

spectra around the [O I] λ6300 line in the stellocentric reference frame. The noisy continuum of V4046 Sgr between −300 and −100 km s^{-1} is due to the challenge in properly subtracting the photospheric absorption from this close binary system.

Following Simon et al. (2016), we fit the minimum number of Gaussian profiles to reproduce the observed lines: first we fit just one Gaussian, and then we compute the rms of the spectrum minus Gaussian at the location of the emission; we add another Gaussian if this rms is larger than twice the rms outside the line. With this approach we find that the spectra of CS Cha,[31] T Cha, and V4046 Sgr can be fit by just one Gaussian profile, while those of MP Mus, TY CrA, T CrA, and VW Cha require two Gaussian profiles. For each component, the FWHM, Gaussian centroid (v_c), and EW are provided in Table 5, together with a classification (Type) that follows Simon et al. (2016). Based on this classification, a component is called LVC (HVC) if the absolute value of the Gaussian velocity centroid is smaller (larger) than 30 km s^{-1}, and, within the LVC, a BC has an FWHM > 40 km s^{-1}, while the NC is narrower. Only VW Cha in this sample has a clearly distinct HVC associated with a jet, while the viewing angle of TY CrA and T CrA is such that most of the [O I] emission is likely from a jet (HVC); see Figure 11 and Appendix B.

To convert the measured EWs into line luminosities, we collect V magnitudes and extinctions (A_V) from the literature, use the source distances in Table 1, and take the flux of a zero-magnitude star in the V band from Bessell (1979), $F_V = 3.1^{-9}$ erg cm^{-2} s^{-1} Å^{-1}. With these inputs the [O I] λ6300 luminosity is calculated as

$$L_{[\mathrm{O\,I}]} = 10^{-(V-Av)/2.5} \times F_V \times \mathrm{EW} \times (4\pi \mathrm{Dist}^2). \quad \text{(A1)}$$

When multiple kinematic components are identified, we provide in Table 1 the total [O I] luminosity obtained from the sum of all components, while the LVC contains the BC and NC contributions.

Appendix B
Notes on Complex Systems

VW Cha is a triple system consisting of a K7 primary (Manara et al. 2017) at 0.″7 from a close, almost equal-mass binary (0.″1 separation; Brandeker et al. 2001; Vogt et al. 2012). The infrared excess is attributed to the primary (Brandeker et al. 2001), which is also the component we focus on in our paper.

V4046 Sgr is a spectroscopic ($P \sim 2.4$ days) binary consisting of two nearly equal-mass stars plus a possible third more distant companion (Donati et al. 2011). The stars are surrounded by a dust disk spatially resolved at millimeter wavelengths: the disk has a large inner hole ($R \sim 30$ au) and extends out to only ∼50 au (Rosenfeld et al. 2013). The gaseous component detected in the ^{12}CO (2–1) and ^{13}CO (2–1) lines is much more extended (out to ∼370 au) and viewed at an inclination of ∼35°, consistent with that assumed to compute the central binary mass (Rodriguez et al. 2010). For the radial velocity of this system, we rely on the precise measurement from the circumbinary CO disk, a systemic LSR velocity of 2.92 ± 0.01 km s^{-1}, which corresponds to a heliocentric velocity of −6.21 km s^{-1}.

[31] After experimenting with different standard stars, we conclude that the extra emission on the red side of the [O I] line is likely due to poor photospheric correction; hence, we do not fit it.

S CrA and VV CrA are two relatively wide binary systems with companions at 1.″3 and 1.″9, respectively (Joy 1945; Koresko et al. 1997; Prato et al. 2003). Given that both systems are variable, Sullivan et al. (2019) use their 2015 infrared flux ratios to define the primary and secondary stars. With this approach, S CrA A is the NW component, while VV CrA A is the southern component. They also determine, for the first time, the spectral type for each star and find similar spectral types in the range K7−M1. As indicated in Table 1, the Keck/HIRES spectra of S CrA covering the [O I] λ6300 line are for the combined (A+B) system: both stars were positioned along the slit, but the MAKEE pipeline extracted the combined flux (Fang et al. 2018). For the VV CrA system, the optical spectrum covered only the primary southern component. In the case of the infrared survey, both binary components were placed along the slit and were extracted separately.

TY CrA is a quadruple system (e.g., Casey et al. 1998; Chauvin et al. 2003): two components form a massive eclipsing double-lined spectroscopic binary with an orbital period of ∼3 days (the primary is a B9 star of 3 $M_\odot$, while the secondary has a mass of 1.6 $M_\odot$); a third spectroscopic component of 1.3 $M_\odot$ orbits around the eclipsing pair at ∼1 au; a fourth more distant (0.″3 ∼ 40 au) visual M-type companion has also been identified. The inclination of the eclipsing binary is ∼85° (Vaňko et al. 2013), while the tertiary is highly inclined with respect to the orbit of the binary (Corporon et al. 1996). The center-of-mass radial velocity for the eclipsing binary is −4.6 km s^{-1} (Casey et al. 1993). We report this value in Table 1 and use it throughout our analysis. The whole system is embedded in a bright reflection nebula; hence, the flux density of TY CrA at infrared wavelengths is rather uncertain. Currie & Sicilia-Aguilar (2011) point out that Spitzer IRAC and MIPS flux densities at wavelengths longer than ∼6 μm are unreliable owing to nebular background emission, hence the lack of a spectral index in our Table 1. Boersma et al. (2009) used a combination of ground-based infrared imaging and spectroscopy to spatially resolve the crowded environment. They infer the presence of a circumstellar disk surrounding all four stars, and thanks to a low-resolution ($R \sim 250$–390) VISIR 1 spectrum, they separate the dust/continuum emission from the more extended PAH emission. It is the dust/continuum emission at 12.9 μm (Figure 5, middle panel in Boersma et al. 2009) that we use here to convert the [Ne II] EW into a line luminosity. TY CrA also sports a strong X-ray emission whose properties agree with the expected combined X-ray emission of the three late-type companions (Forbrich & Preibisch 2007).

T CrA is an F-type star that might have a companion at >0.″14 according to spectroastrometry in the Hα line (Bailey 1998; Takami et al. 2003). However, no companion has been detected using spectroastrometry in the fundamental rovibrational band of CO at 4.6 μm (Pontoppidan et al. 2011), nor with K-band speckle imaging (e.g., Köhler et al. 2008). Wang et al. (2004) identified a Herbig–Haro knot close to T CrA, hinting at the presence of a jet. More recently, A. Whelan et al. (2020, in preparation) discovered, through spectroastrometry in the [O I] and other optical forbidden lines, that the jet is nearly in the plane of the sky. This means that the flared, massive disk surrounding T CrA (Sicilia-Aguilar et al. 2013; Cazzoletti et al. 2019) is likely seen almost edge-on.

CS Cha is a single-line spectroscopic binary with a companion mass of at least 0.1 $M_\odot$ and a period longer than 2482 days (Guenther et al. 2007). Its SED hinted early on at the

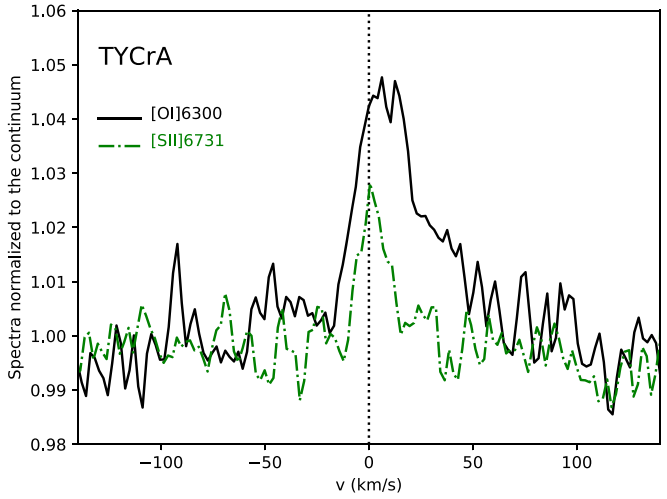

Figure 11. Comparison of the [O I] λ6300 (black solid) and the [S II] λ6731 (green dotted–dashed) profiles for TY CrA. As [S II] λ6731 has a critical density two orders of magnitude lower than the [O I] λ6300 transition, it is sensitive to jet emission. The figure illustrates that the LVC [O I] λ6300 is contaminated by jet emission.

presence of a large dust cavity (Gauvin & Strom 1992), which has been recently imaged at millimeter wavelengths with ALMA (Francis & van der Marel 2020). SPHERE polarized imagery identified an additional faint companion at a projected separation of 210 au, outside the circumbinary disk of the primary (Ginski et al. 2018). Our high-resolution optical and infrared spectra focus on the CS Cha spectroscopic binary and its disk.

Figure 11 shows a comparison of the [O I] λ6300 and the [S II] λ6731 profiles for TY CrA.

Appendix C
Comparison of VISIR and Spitzer [Ne II] Fluxes

Here we compare the [Ne II] 12.81 μm fluxes obtained from the Spitzer/IRS medium-resolution spectra (slit width 4.″7) with those recovered with the much narrower slits of VISIR 1 ($\sim$0.″4) and VISIR 2 (0.″75) for the targets in Table 1. Except for TWA 3A, V4046 Sgr, S CrA, T CrA, TY CrA, and VV CrA, all Spitzer [Ne II] fluxes can be found in the following papers: Pascucci et al. (2007), Güdel et al. (2010), and Rigliaco et al. (2015). TY CrA was not observed with Spitzer/IRS. For the other five sources we retrieve reduced Spitzer spectra from the online CASSIS database (Lebouteiller et al. 2015), and, following Rigliaco et al. (2015), we fit a Gaussian profile when the [Ne II] transition is detected (for V4046 Sgr and T CrA) or calculate a 3σ upper limit when it is not detected (for TWA 3A, S CrA, and VV CrA).

The left panel of Figure 12 compares the Spitzer (blue) and VISIR (black) fluxes (circles) or upper limits (downward-pointing triangles) for each source. For TY CrA (# 18) we only show the VISIR detection. There are a total of 11 sources with Spitzer and VISIR [Ne II] fluxes (Group 1); 8 with a Spitzer flux but no VISIR detection (Group 2: GI Tau, IM Lup, RNO 90, Wa Oph6, LkCa 15, Sz 102, DoAr 44, RX J1842.9–35); 5 with a VISIR flux but no Spitzer detection (Group 3: V836 Tau, RY Lup, SR 21, SCr A, MP Mus); and 6 sources that do not show an [Ne II] detection in the VISIR or in the Spitzer spectrum (Group 4: DO Tau, DR Tau, TWA 3A, GQ Lup, VV CrA, VZ Cha). Except for TWA 3A, the VISIR upper limits are more stringent than the Spitzer ones. Excluding Group 4 sources, we also show in the right panel of Figure 12 the Spitzer-to-VISIR line flux ratios versus the source infrared spectral index (n_{13-31}): circles are used for Group 1 sources, upward-pointing triangles for Group 2, and downward-pointing triangles for Group 3 sources. A black filled circle identifies objects with a jet (HVC) detected in the [O I] λ6300 transition, basically all Table 1 sources with $L_{[\mathrm{O\,I}]_{\mathrm{tot}}} > L_{[\mathrm{O\,I}]_{\mathrm{LVC}}}$. Sources with jets belong predominantly to Groups 1 and 2, and, as expected, their Spitzer flux is typically larger than the VISIR flux because of spatially extended [Ne II] emission from the jet that is filtered out by the narrower slits of VISIR (see also Sacco et al. 2012, Figure 4 for a similar behavior in Class I sources). The Spitzer nondetections of Group 3 sources are likely due to a combination of high infrared continuum and poor spectral resolution for the IRS, which reduces the line-to-continuum ratio. Finally, sources with no jets and $n_{13-31} \gtrsim 1$ have Spitzer fluxes well within a factor of 2 of the VISIR ones. This suggests that only Spitzer/IRS sources with significant dust depletion in their inner disk and no HVC in the [O I] λ6300 line should be used to further expand the VISIR sample.

With this result in mind, we cross-matched the sample of sources observed at high spectral resolution that have only a [O I] λ6300 LVC detection (Simon et al. 2016; Fang et al. 2018; Banzatti et al. 2019) with published and archival Spitzer/IRS spectra from sources with $n_{13-31} \gtrsim 1$. We only find five additional targets, all of them well-known disks with dust cavities; see Table 6 and Figure 5 in the main text.

Table 6
Spitzer/IRS Sources with Depleted Inner Dust Disks That Can Be Used to Expand the VISIR Sample

Target	n_{13-31}	Log $L_{[\mathrm{Ne\,II}]}$	Log $L_{[\mathrm{O\,I}]_{\mathrm{LVC}}}$	References
CoKuTau4	2.27	−5.57	−5.55	1, 2
DM Tau	1.3	−5.45	−5.68	3, 4
GMAur	1.8	−5.09	−4.55	3, 2
UXTauA	1.7	−5.26	−4.69	3, 4
RX J1852.33700	2.47	−5.32	−5.34	3, 5, 4

References. (1) this work; (2) Simon et al. 2016; (3) Rigliaco et al. 2015; (4) Fang et al. 2018; (5) Pascucci et al. 2007.

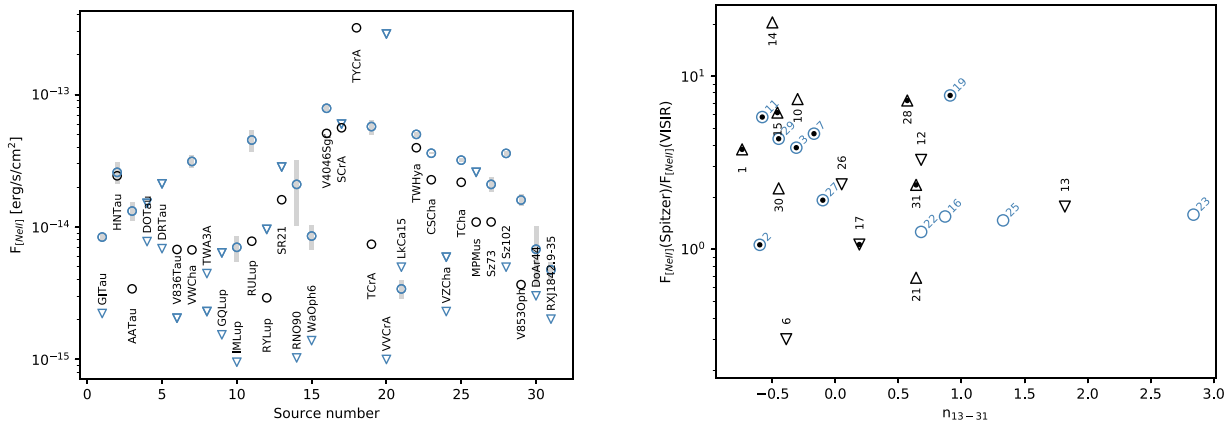

Figure 12. Left panel: comparison of Spitzer/IRS (blue) and VISIR 1 and VISIR 2 (black) [Ne II] fluxes for all sources in Table 1. Detections are shown with circles, while 3σ upper limits are shown with downward-pointing triangles. Gray bars show the 1σ uncertainty on the Spitzer fluxes. Right panel: [Ne II] Spitzer-to-VISIR line ratios vs. source infrared spectral index. Sources with detections in Spitzer and VISIR spectra are shown with circles, detections only in the Spitzer spectra with upward-pointing triangles, and detections only in the VISIR spectra with downward-pointing triangles. A black filled circle identifies sources with [O I] λ6300 HVC emission.

ORCID iDs

Ilaria Pascucci https://orcid.org/0000-0001-7962-1683
Andrea Banzatti https://orcid.org/0000-0003-4335-0900
Uma Gorti https://orcid.org/0000-0002-3311-5918
Min Fang https://orcid.org/0000-0001-8060-1321
Klaus Pontoppidan https://orcid.org/0000-0001-7552-1562
Richard Alexander https://orcid.org/0000-0001-6410-2899
Suzan Edwards https://orcid.org/0000-0002-3232-665X
Colette Salyk https://orcid.org/0000-0003-3682-6632
Ettore Flaccomio https://orcid.org/0000-0002-3638-5788
Geoffrey A. Blake https://orcid.org/0000-0003-0787-1610
Cassandra Hall https://orcid.org/0000-0002-8138-0425
Inga Kamp https://orcid.org/0000-0001-7455-5349
Hans Ulrich Käufl https://orcid.org/0000-0002-8806-9795
Gwendolyn Meeus https://orcid.org/0000-0002-6251-0108
Michael Meyer https://orcid.org/0000-0003-1227-3084
Tyler Pauly https://orcid.org/0000-0001-9500-9267
Michael Sterzik https://orcid.org/0000-0002-5784-4437

References

Acke, B., van den Ancker, M. E., & Dullemond, C. P. 2005, A&A, 436, 209
Akritas, Michael G., Murphy, Susan A., & Lavalley, Michael P. 1995, J. Am. Stat. Assoc., 90, 170
Alcalá, J. M., Manara, C. F., Natta, A., et al. 2017, A&A, 600A, 20
Alexander, R., Pascucci, I., Andrews, S., et al. 2014, in Protostars and Planets VI, ed. H. Beuther et al. (Tucson, AZ: Univ. Arizona Press), 475
Alexander, R. D. 2008, MNRAS, 391L, 64
Andrews, S. M., Wilner, D. J., Zhu, Z., et al. 2016, ApJ, 820L, 40
Ansdell, M., Williams, J. P., van der Marel, N., et al. 2016, ApJ, 828, 46
Aresu, G., Meijerink, R., Kamp, I., et al. 2012, A&A, 547A, 69
Armitage, P. J. 2011, ARA&A, 49, 195
Astropy Collaboration, Price-Whelan, A. M., Sipőcz, B. M., et al. 2018, AJ, 156, 123
Astropy Collaboration, Robitaille, T. P., Tollerud, E. J., et al. 2013, A&A, 558, A33
Bai, Xue-Ning 2016, ApJ, 821, 80
Bailer-Jones, C. A. L., Rybizki, J., Fouesneau, M., et al. 2018, AJ, 156, 58
Bailey, J. 1998, MNRAS, 301, 161
Balbus, S. A., & Hawley, J. F. 1991, ApJ, 376, 214
Baldovin-Saavedra, C., Audard, M., Carmona, A., et al. 2012, A&A, 543A, 30
Ballabio, G., Alexander, R. D., & Clarke, C. J. 2020, MNRAS, 496, 2932
Banzatti, A., Meyer, M. R., Manara, C. F., et al. 2014, ApJ, 780, 26
Banzatti, A., Pascucci, I., Edwards, S., et al. 2019, ApJ, 870, 76
Banzatti, A., & Pontoppidan, K. M. 2015, ApJ, 809, 167
Banzatti, A., Pontoppidan, K. M., Salyk, C., et al. 2017, ApJ, 834, 152
Baraffe, I., Homeier, D., Allard, F., & Chabrier, G. 2015, A&A, 577A, 42
Bessell, M. S. 1979, PASP, 91, 589
Blandford, R. D., & Payne, D. G. 1982, MNRAS, 199, 883
Boersma, C., Peeters, E., Martín-Hernández, N. L., et al. 2009, A&A, 502, 175
Bouvier, J., Chelli, A., Allain, S., et al. 1999, A&A, 349, 619
Brandeker, A., Liseau, R., Artymowicz, P., & Jayawardhana, R. 2001, ApJ, 561L, 199
Cahill, E., Whelan, E. T., Huélamo, N., et al. 2019, MNRAS, 484, 4315
Casey, B. W., Mathieu, R. D., Suntzeff, N. B., et al. 1993, AJ, 105, 2276
Casey, B. W., Mathieu, R. D., Vaz, L. P. R., et al. 1998, AJ, 115, 1617
Cazzoletti, P., Manara, C. F., Baobab Liu, H., et al. 2019, A&A, 626A, 11
Chauvin, G., Lagrange, A.-M., Beust, H., et al. 2003, A&A, 406L, 51
Clarke, C. J., & Alexander, R. D. 2016, MNRAS, 460, 3044
Corporon, P., Lagrange, A. M., & Beust, H. 1996, A&A, 310, 228
Curran, R. L., Argiroffi, C., Sacco, G. G., et al. 2011, A&A, 526A, 104
Currie, T., & Sicilia-Aguilar, A. 2011, ApJ, 732, 24
de Juan Ovelar, M., Pinilla, P., Min, M., et al. 2016, MNRAS, 459L, 85
Dionatos, O., Woitke, P., Güdel, M., et al. 2019, A&A, 625A, 66
Donati, J.-F., Gregory, S. G., Montmerle, T., et al. 2011, MNRAS, 417, 1747
Dong, R., Najita, J. R., & Brittain, S. 2018, ApJ, 862, 103
Dzib, S. A., Loinard, L., Ortiz-León, G. N., Rodríguez, L. F., & Galli, P. A. B. 2018, ApJ, 867, 151
Ercolano, B., Drake, J. J., Raymond, J. C., & Clarke, C. C. 2008, ApJ, 688, 398
Ercolano, B., & Owen, J. E. 2010, MNRAS, 406, 1553
Ercolano, B., & Pascucci, I. 2017, RSOS, 4, 170114
Espaillat, C., Calvet, N., D'Alessio, P., et al. 2007, ApJL, 664, L111
Espaillat, C., Furlan, E., D'Alessio, P., et al. 2011, ApJ, 728, 49
Espaillat, C., Ingleby, L., & Furlan, E. 2013, ApJ, 762, 62
Fang, M., Pascucci, I., Edwards, S., et al. 2018, ApJ, 868, 28
Flaherty, K., Hughes, A. M., Simon, J. B., et al. 2020, ApJ, 895, 109
Flaherty, K. M., Hughes, A. M., Rose, S. C., et al. 2017, ApJ, 843, 150
Forbrich, J., & Preibisch, T. 2007, A&A, 475, 959
Francis, L., & van der Marel, N. 2020, ApJ, 892, 111
Frank, A., Ray, T. P., & Cabrit, S. 2014, in Protostars and Planets VI, ed. H. Beuther et al. (Tucson, AZ: Univ. Arizona Press), 451
Furlan, E., Watson, D. M., McClure, M. K., et al. 2009, ApJ, 703, 1964
Garcia, P. J. V., Cabrit, S., Ferreira, J., & Binette, L. 2001, A&A, 377, 609
Garcia Lopez, R., Natta, A., Testi, L., & Habart, E. 2006, A&A, 459, 837
Gauvin, L. S., & Strom, K. M. 1992, ApJ, 385, 217
Ginski, C., Benisty, M., van Holstein, R. G., et al. 2018, A&A, 616A, 79
Glassgold, A. E., Najita, J. R., & Igea, J. 2007, ApJ, 656, 515
Gorti, U., Liseau, R., Sándor, Z., & Clarke, C. 2016, SSRv, 205, 125
Gressel, O., Ramsey, J. P., Brinch, Ch., et al. 2020, ApJ, 896, 126
Gressel, O., Turner, N. J., Nelson, R. P., & McNally, C. P. 2015, ApJ, 801, 84
Güdel, M., Lahuis, F., Briggs, K. R., et al. 2010, A&A, 519A, 113
Guenther, E. W., Esposito, M., Mundt, R., et al. 2007, A&A, 467, 1147
Hartigan, P., Edwards, S., & Ghandour, L. 1995, ApJ, 452, 736
Hartigan, P., Morse, J. A., & Raymond, J. 1994, ApJ, 436, 125
Hartigan, P., Raymond, J., & Hartmann, L. 1987, ApJ, 316, 323
Helsel, D. R. 2005, Nondectects and Data Analysis; Statistics for censored environmental data (Hoboken, NJ: John Wiley & Sons)
Hendler, N., Pascucci, I., Pinilla, P., et al. 2020, ApJ, 895, 126
Hendler, N. P., Pinilla, P., Pascucci, I., et al. 2018, MNRAS, 475L, 62

Herczeg, G. J., & Hillenbrand, L. A. 2014, ApJ, 786, 97
Hollenbach, D., & Gorti, U. 2009, ApJ, 703, 1203
Hollenbach, D., & McKee, C. F. 1979, ApJS, 41, 555
Joy, A. H. 1945, ApJ, 102, 168
Kastner, J. H., Hily-Blant, P., Sacco, G. G., Forveille, T., & Zuckerman, B. 2010, ApJL, 723, L248
Kastner, J. H., Principe, D. A., Punzi, K., et al. 2016, AJ, 152, 3
Kellogg, K., Prato, L., Torres, G., et al. 2017, ApJ, 844, 168
Kimmig, C. N., Dullemond, C. P., & Kley, W. 2020, A&A, 633A, 4
Köhler, R., Neuhäuser, R., Krämer, S., et al. 2008, A&A, 488, 997
Kóspál, Á, Ábrahám, P., Acosta-Pulido, J. A., et al. 2012, ApJS, 201, 11
Koresko, C. D., Herbst, T. M., & Leinert, C. 1997, ApJ, 480, 741
Kwan, J., & Tademaru, E. 1995, ApJ, 454, 382
Lebouteiller, V., Barry, D. J., Goes, C., et al. 2015, ApJS, 218, 21
Loomis, R. A., Öberg, K. I., Andrews, S. M., & MacGregor, M. A. 2017, ApJ, 840, 23
Louvet, F., Dougados, C., Cabrit, S., et al. 2016, A&A, 596A, 88
Mamajek, E. E., Meyer, M. R., & Liebert, J. 2002, AJ, 124, 1670
Manara, C. F., Testi, L., Herczeg, G. J., et al. 2017, A&A, 604A, 127
McClure, M. K., Espaillat, C., Calvet, N., et al. 2015, ApJ, 799, 162
McGinnis, P., Dougados, C., Alencar, S. H. P., et al. 2018, A&A, 620A, 87
Moré, J. J., & Wright, S. 1987, Optimization Software Guide (Philadelphia, PA: SIAM)
Najita, J. R., Carr, J. S., Strom, S. E., et al. 2010, ApJ, 712, 274
Najita, J. R., Doppmann, G. W., Bitner, M. A., et al. 2009, ApJ, 697, 957
Natta, A., Testi, L., Alcalá, J. M., et al. 2014, A&A, 569A, 5
Nisini, B., Antoniucci, S., Alcalá, J. M., et al. 2018, A&A, 609A, 87
Ogihara, M., Kokubo, E., Suzuki, T. K., & Morbidelli, A. 2018, A&A, 615A, 63
Pascucci, I., Edwards, S., Heyer, M., et al. 2015, ApJ, 814, 14
Pascucci, I., Hollenbach, D., Najita, J., et al. 2007, ApJ, 663, 383
Pascucci, I., Ricci, L., Gorti, U., et al. 2014, ApJ, 795, 1
Pascucci, I., & Sterzik, M. 2009, ApJ, 702, 724
Pascucci, I., Sterzik, M., Alexander, R. D., et al. 2011, ApJ, 736, 13
Pascucci, I., Testi, L., Herczeg, G. J., et al. 2016, ApJ, 831, 125
Pelletier, G., & Pudritz, R. E. 1992, ApJ, 394, 117
Picogna, G., Ercolano, B., Owen, J. E., & Weber, M. L. 2019, MNRAS, 487, 691
Pontoppidan, K. M., Blake, G. A., & Smette, A. 2011, ApJ, 733, 84
Pontoppidan, K. M., Salyk, C., Blake, G. A., et al. 2010, ApJ, 720, 887
Prato, L., Greene, T. P., & Simon, M. 2003, ApJ, 584, 853
Ray, T., Dougados, C., Bacciotti, F., Eislöffel, J., & Chrysostomou, A. 2007, in Protostars and Planets V, ed. B. Reipurth et al. (Tucson, AZ: Univ. Arizona Press), 231
Rigliaco, E., Pascucci, I., Duchene, G., et al. 2015, ApJ, 801, 31
Rigliaco, E., Pascucci, I., Gorti, U., et al. 2013, ApJ, 772, 60
Roccatagliata, V., Sacco, G. G., Franciosini, E., & Randich, S. 2018, A&A, 617, L4
Rodriguez, D. R., Kastner, J. H., Wilner, D., & Qi, C. 2010, ApJ, 720, 1684
Rosenfeld, K. A., Andrews, S. M., Wilner, D., et al. 2013, ApJ, 775, 136
Sacco, G. G., Flaccomio, E., Pascucci, I., et al. 2012, ApJ, 747, 142
Safier, P. N. 1993, ApJ, 408, 115
Salyk, C., Lacy, J. H., Richter, M. J., et al. 2015, ApJ, 810L, 24
Schisano, E., Covino, E., Alcalá, J. M., et al. 2009, A&A, 501, 1013
Shang, H., Glassgold, A. E., Lin, W.-C., & Liu, C.-F. J. 2010, ApJ, 714, 1733
Shu, F., Najita, J., Ostriker, E., et al. 1994, ApJ, 429, 781
Sicilia-Aguilar, A., Henning, T., Linz, H., et al. 2013, A&A, 551A, 34
Simon, J. B., Bai, X.-N., Flaherty, K. M., & Hughes, A. M. 2018, ApJ, 865, 10
Simon, M., Guilloteau, S., Di Folco, E., et al. 2017, ApJ, 844, 158
Simon, M. N., Pascucci, I., Edwards, S., et al. 2016, ApJ, 831, 169
Skinner, S. L., & Güdel, M. 2017, ApJ, 839, 45
Sullivan, K., Prato, L., Edwards, S., Avilez, I., & Schaefer, G. H. 2019, ApJ, 884, 28
Szulágyi, J., Pascucci, I., Ábrahám, P., et al. 2012, ApJ, 759, 47
Takami, M., Bailey, J., & Chrysostomou, A. 2003, A&A, 397, 675
Teague, R., Guilloteau, S., Semenov, D., et al. 2016, A&A, 592A, 49
Torres, C. A. O., Quast, G. R., da Silva, L., et al. 2006, A&A, 460, 695
Tripathi, A., Andrews, S. M., Birnstiel, T., & Wilner, D. J. 2017, ApJ, 845, 44
Turner, N. J., Fromang, S., Gammie, C., et al. 2014, in Protostars and Planets VI, ed. H. Beuther et al. (Tucson, AZ: Univ. Arizona Press), 411
van der Marel, N., Verhaar, B. W., van Terwisga, S., et al. 2016, A&A, 592, A126
Vaňko, M., Eiff, M. A.-v., Pribulla, T., et al. 2013, MNRAS, 431, 2230
Vioque, M., Oudmaijer, R. D., Baines, D., Mendigutía, I., & Pérez-Martínez, R. 2018, A&A, 620A, 128
Vogt, N., Schmidt, T. O. B., Neuhäuser, R., et al. 2012, A&A, 546A, 63
Wang, H., Mundt, R., Henning, T., et al. 2004, ApJ, 617, 1191
Weber, M. L., Ercolano, B., Picogna, G., Hartmann, L., & Rodenkirch, P. J. 2020, MNRAS, 496, 223
Zhu, Z., Nelson, R. P., Dong, R., et al. 2012, ApJ, 755, 6